

# Negative Autoregulation Matches Production and Demand in Synthetic Transcriptional Networks

Elisa Franco,<sup>\*,†</sup> Giulia Giordano,<sup>‡</sup> Per-Ola Forsberg,<sup>§</sup> and Richard M. Murray<sup>||</sup><sup>†</sup>Mechanical Engineering, University of California at Riverside, Riverside, California 92521, United States<sup>‡</sup>Mathematics and Computer Science, University of Udine, 33100 Udine, Italy<sup>§</sup>Kristianstad Central Hospital, 29832 Tollarp, Sweden<sup>||</sup>Engineering and Applied Science, California Institute of Technology, Pasadena, California 91125, United States

## Supporting Information

**ABSTRACT:** We propose a negative feedback architecture that regulates activity of artificial genes, or “genelets”, to meet their output downstream demand, achieving robustness with respect to uncertain open-loop output production rates. In particular, we consider the case where the outputs of two genelets interact to form a single assembled product. We show with analysis and experiments that negative autoregulation matches the production and demand of the outputs: the magnitude of the regulatory signal is proportional to the “error” between the circuit output concentration and its actual demand. This two-device system is experimentally implemented using *in vitro* transcriptional networks, where reactions are systematically designed by optimizing nucleic acid sequences with publicly available software packages. We build a predictive ordinary differential equation (ODE) model that captures the dynamics of the system and can be used to numerically assess the scalability of this architecture to larger sets of interconnected genes. Finally, with numerical simulations we contrast our negative autoregulation scheme with a cross-activation architecture, which is less scalable and results in slower response times.

**KEYWORDS:** negative feedback, nucleic acid systems, transcriptional circuits, synthetic biology, *in vitro*

Our increased understanding of biological parts enables their use in a variety of new applications<sup>1</sup> of growing complexity, ranging from nanofabrication to drug production and delivery. When a large number of molecular devices are required to operate together within a system to achieve an overall functionality, it is essential that the output of each device is automatically tuned to meet its demand. For instance, a synthetic circuit producing an unregulated, excessive amount of non-native products in a host may cause overloading and reduce growth.<sup>2–4</sup> Again, insufficient production of key components within an engineered circuit may hinder its overall performance. These phenomena are typically present in complex metabolic pathways transferred from their native host to more cost-effective microorganisms: the production of individual enzymes must be carefully engineered and balanced to guarantee correct operation.<sup>5</sup> In the context of nanotechnology, recently demonstrated RNA nanostructures require the presence of stoichiometrically controlled concentrations of individual strands; RNA transcription speed imbalances may result in the formation of undesired complexes and incorrect assemblies, both *in vitro*<sup>6</sup> and *in vivo*.<sup>7</sup> In other words, the functionality of a large scale synthetic system may deteriorate if the input/output behaviors of individual modules characterized in isolation do not automatically meet specifications in their network context. Rather than fine-tuning a device to fit a range of contingent network demands, it is desirable to identify

design principles that would automatically ensure a demand-adaptive operation.

In traditional engineering fields, the challenge of adapting the output behavior of a device to reach the desired operating point is met by routinely employing negative feedback at a variety of scales (from individual transistors to layered network control systems). Consider, for instance, a device *S* whose output *y* is required to track a reference *r*, a signal which may fluctuate over time (Figure 1A). A negative feedback loop causes the input to the regulated process *S* to be proportional with opposite sign to the error *e* between the output *y* and the reference value *r*.

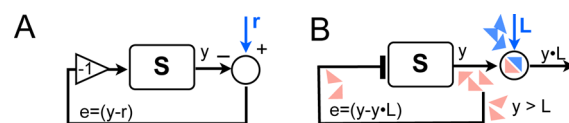


**Figure 1.** (A) General structure of a negative feedback loop, where the system input counteracts the error between the desired and actual system output. (B) Negative feedback scheme for a molecular system, where an excess production of *y* is used to downregulate the “activity” of the system.

Special Issue: IWBD 2013

Received: October 4, 2013

Published: February 26, 2014

Thus, the system's response is always driven by an input with opposite trend relative to the error  $e$ . For instance, if  $y$  exceeds  $r$  then the error is positive, but the input to  $S$  is negative and drives "down" the response of  $S$ . In addition to maintaining a desired output level, negative feedback generally gives us the ability to redesign the dynamics of a system, and improve its robustness with respect to parametric uncertainty.<sup>8</sup>

Negative feedback is ubiquitous in biomolecular networks. For example, negative autoregulation is a motif present in over 40% of genes in *E. coli*.<sup>9,10</sup> This mechanism is associated with proteins that are generally in low demand,<sup>11,12</sup> and reduces noise<sup>13–15</sup> and mutation rates<sup>16</sup> in gene expression profiles. In the context of synthetic biology, negative autoregulation has been used to achieve faster response speed<sup>17</sup> and to improve robustness.<sup>13,16</sup> The development of novel, tunable repression mechanisms promises to improve our ability to control dynamics and manage noise of increasingly complex molecular circuits both in cellular hosts<sup>18,19</sup> and in cell-free systems.<sup>20–22</sup> However, the use of negative feedback to match production and demand within a biochemical reaction network has, to our knowledge, not been demonstrated.

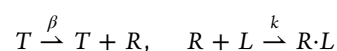
In this paper, we propose to use negative feedback to accurately regulate activity of components so they can meet their output downstream demand, achieving robustness with respect to uncertain open-loop (*i.e.*, in the absence of feedback) output production rates. Figure 1B shows a scheme of this feedback architecture, which closely mimics the structure of a typical negative feedback circuit in electrical or mechanical systems. The output  $y$  of component  $S$  binds to a downstream target  $L$ , which represents the demand for  $y$ ; we design a negative feedback pathway to use excess  $y$  (not bound to  $L$ ) to reduce its own production rate: thus, the magnitude of the regulatory signal is proportional to the "error" between the circuit output concentration and its actual demand. If, in turn,  $L$  is the output of another circuit, it is conceivable that a negative feedback loop in each individual module would help matching production and demand in the overall system. With analysis and experiments we show that this expectation is correct, and negative autoregulation yields matching output fluxes in both circuits.

The two-module system is implemented using *in vitro* transcriptional circuits,<sup>20,23,24</sup> a versatile toolbox to program and build dynamic behaviors using nucleic acid reaction networks. Within the general context of cell-free systems,<sup>25</sup> this platform allows to rapidly engineer molecular functions in a controlled environment with reduced uncertainty. We designed two synthetic genes to transcribe RNA outputs that bind to form a complex; each RNA species is also designed to downregulate its own production through promoter displacement.<sup>20</sup> Thus, excess of either species modulates the genes' activity and achieves matched promoter activity levels. The product formation reaction and the inhibitory pathways are systematically engineered by optimizing nucleic acid sequence complementarity domains, using publicly available software packages.<sup>26,27</sup> We build a predictive ordinary differential equation (ODE) model that captures the dynamics of the system and can be used to numerically assess the scalability of this architecture to larger sets of interconnected genes. Finally, with numerical simulations, we contrast the performance of our negative autoregulation scheme with the behavior of a cross-activation architecture, which is less scalable and results in slower response times. This work builds on preliminary numerical analysis and experiments on transcription matching

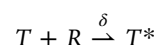
synthetic systems.<sup>28–31</sup> (Preliminary results related to this manuscript were published in a series of conference manuscripts. The two-genelet transcription rate matching system was described in Franco et al.,<sup>28</sup> which includes preliminary numerical analysis and data; a parametric numerical analysis contrasting the negative and positive feedback schemes was shown in Franco et al.<sup>29</sup> Finally, the simple model for the system and the scalability of its performance were initially considered in Giordano et al.<sup>30</sup>) We foresee that systematic use of similar negative feedback architectures will play a major role in the scalability of *in vitro* biomolecular systems, including logic,<sup>32</sup> dynamic,<sup>24</sup> and self-assembly networks.<sup>6,33</sup>

## RESULTS

**Negative Feedback Can Modulate Activity to Meet Downstream Demand.** We begin by considering a simple model problem: a molecule  $R$  is produced by species  $T$ , and binds to a target  $L$ .



These reactions may represent, for instance, RNA or protein production followed by binding of the product to a downstream binding site or ligand. In the absence of any regulatory pathway feeding back to  $T$  information regarding the effective "consumption" of  $R$  by the target  $L$ , the production and demand of  $R$  are not automatically matched: thus, an excess of unused  $R$  may accumulate in solution for regimes where the demand does not exceed the maximum production rates. However, if we program a reaction



whereby species  $T$  bound to  $R$  becomes an inactive species  $T^*$ , we introduce a negative feedback mechanism that is proportional to the unused amount of  $[R] \propto [R^{\text{tot}}] - [R \cdot L]$ , thus proportional to the error between production and demand. The scheme is represented in Figure 2A. Assuming that the concentration of the "demand" species  $L$  is constant, that the total amount of  $T$  is constant ( $[T] + [T^*] = [T^{\text{tot}}]$ ), and finally that inactive  $T^*$  spontaneously reverts to its active state at a certain rate  $\alpha$ ,  $T^* \xrightarrow{\alpha} T$ , the system is described by the following set of ODEs:

$$\frac{d[T]}{dt} = \alpha([T^{\text{tot}}] - [T]) - \delta[T][R] \quad (1)$$

$$\frac{d[R]}{dt} = \beta[T] - \delta[T][R] - k[L][R] \quad (2)$$

For illustrative purposes, we numerically simulate these differential equations, choosing nominal parameters  $[T^{\text{tot}}] = 100 \text{ nM}$ ,  $\alpha = 3 \times 10^{-4} \text{ s}^{-1}$ ,  $\beta = 0.1 \text{ s}^{-1}$ ,  $k = 2 \times 10^{-3} \text{ M}^{-1} \text{ s}^{-1}$ ,  $\delta = 5 \times 10^2 \text{ M}^{-1} \text{ s}^{-1}$ ; these concentrations and rates are within a realistic range for *in vitro* reaction systems.<sup>24,25</sup> In Figure 2, we explore the steady state behavior of the system as a function of the feedback parameter  $\delta$ , the total amount of load  $L$ , and the total concentration of generating species  $T$ . First, as shown in Figure 2B, we note that a suitably high feedback rate  $\delta$  reduces the steady state fraction of unused output  $[R]/[R^{\text{tot}}]$  (output not bound to its load): this means waste in the system is reduced. In addition, for a given, large  $\delta$ , a significant variation in load results in a moderate variation in the fraction of unused output: this behavior is consistent with the role of high feedback in reducing load sensitivity in retroactivity theory.<sup>34</sup> In Figure 2C,

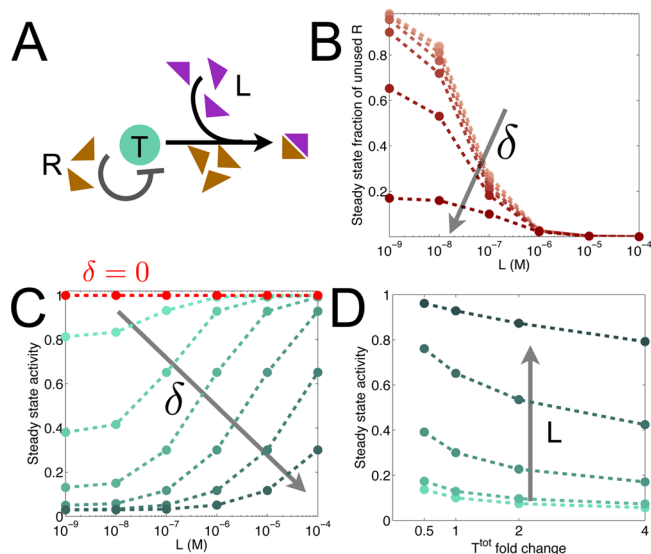
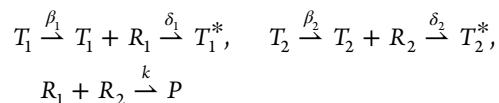


**Figure 2.** (A) Scheme of negative feedback where output  $R$  not bound to the target load  $L$  is used to downregulate its production. (B) The steady state fraction ( $[R^{\text{free}}]/[R^{\text{tot}}]$ ) of unused  $R$  as a function of the downstream load is reduced using a high negative feedback rate  $\delta$ . (C) The steady state activity ( $[T]/[T^{\text{tot}}]$ ) of the genelet as a function of the downstream load is reduced by an increase in the negative feedback rate  $\delta$ . (D) The steady state activity of the genelet as a function of the total genelet concentration is increased using a higher downstream load. In panels B and D, we considered  $\delta = 0, 5, 50, 5 \times 10^2, 5 \times 10^3, 5 \times 10^4, 5 \times 10^5$  M/s. In panel D, the nominal concentration of  $[T^{\text{tot}}]$  is 100 nM, and the load was varied as  $[L] = 1, 10, 10^2, 10^3, 10^4$  nM.

we observe that in the presence of feedback the activity of the generating species, defined as  $[T]/[T^{\text{tot}}]$ , is modulated by the demand  $L$ . Finally, Figure 2D shows that the presence of negative feedback yields closed loop activity levels that (given a certain demand) are robust with respect to uncertainty in  $[T^{\text{tot}}]$ , which is a simple open-loop knob to scale the production rate of  $R$ .

#### Matching Output Fluxes of Interconnected Devices.

In many practical cases, several molecular species in a network bind stoichiometrically to form an overall product. For instance, these species could be RNA strands<sup>6</sup> or proteins<sup>35</sup> self-assembling in a nanostructure. To avoid excess production and accumulation of any participating species, we can use the negative feedback scheme described above. For simplicity, we begin by considering a network where two generating species  $T_1$  and  $T_2$  produce assembling outputs that self-inhibit according to the following reactions:



where  $P$  is an assembled product, and again, we assume that the total amount of the generating species is conserved,  $[T_i^{\text{tot}}] = T_i + T_i^*, i = 1, 2$ . The dynamics of  $[T_1]$  and  $[T_2]$  are thus described by ODEs identical to eq 1, while the dynamics of  $[R_i]$  become

$$\frac{d[R_i]}{dt} = \beta_i[T_i] - \delta_i[R_i][T_i] - k[R_i][R_j], \quad i = 1, 2$$

Example solutions to these ODEs are shown in Figure 4A, where for the two subsystems we chose identical parameters, consistent with our previous simulations at Figure 2 ( $\alpha_1 = \alpha_2 =$

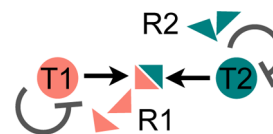


**Figure 3.** Our two-device negative feedback architecture.

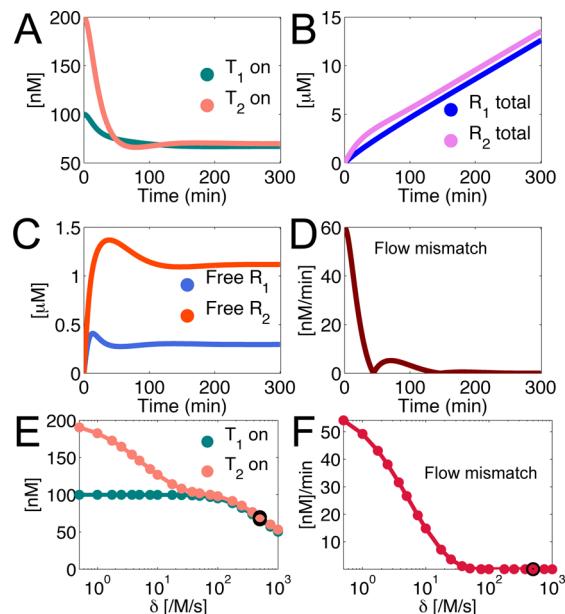


**Figure 4.** (A–D) Numerical simulations showing example trajectories for the two-component negative feedback architecture. (A) Time course of active  $T_1$  and  $T_2$ . (B) Time course of total produced outputs  $R_1$  and  $R_2$ . (C) Time course of unbound  $R_1$  and  $R_2$ . (D) Time course for the flux mismatch in the production of total  $R_1$  and  $R_2$ . (E) Steady state activity of  $T_1$  and  $T_2$  as a function of the negative feedback parameter  $\delta$ . (F) Mismatch in the flux of  $R_1$  and  $R_2$  as a function of  $\delta$ . The dark circle in panels E and F marks the nominal conditions used for the time courses plotted in panels A–D.

$\alpha = 3 \times 10^{-4}$ /s, and similarly defined  $\beta = 0.1$ /s,  $k = 2 \times 10^{-3}$ /M·s,  $\delta = 5 \times 10^2$ /M·s).

Expressions for the nullclines of the system are derived in section 2.1 of the Supporting Information (SI), the equilibria (intersections of the nullclines) are numerically evaluated as a function of the negative feedback reaction. At steady state, the concentration of active  $T_1$  is nearly identical to the active concentration of  $T_2$ . Figure 4E, however, shows that this property breaks down when the negative feedback rate  $\delta$  is too low; while a high  $\delta$  guarantees matched activity levels, it also causes an overall lower activity level for the system and pushes down the production of the  $P = R_1 \cdot R_2$  complex. (We define mean steady state activity as the mean active  $[T_i]$  during the last hour of a 10 h trajectory simulation.)

We also ask if, at a stationary regime, the dynamic behaviors of  $R_1$  and  $R_2$  are similar. We find that the flux of both outputs are identical when the active concentrations  $[\bar{T}_1]$  and  $[\bar{T}_2]$  are related as follows (cf. section 2.1 of the SI):

$$\bar{T}_2 = \bar{T}_1 + \frac{\alpha}{\alpha + \beta}(T_2^{\text{tot}} - T_1^{\text{tot}}) \quad (3)$$

where for simplicity we assumed  $\alpha_1 = \alpha_2 = \alpha$ ,  $\beta_1 = \beta_2 = \beta$ , and  $\delta_1 = \delta_2 = \delta$ . Thus, when  $\beta$  is sufficiently large relative to  $\alpha$ , the flux of the two outputs is matched. The steady state flux mismatch is plotted as a function of  $\delta$  in Figure 3F. We observe

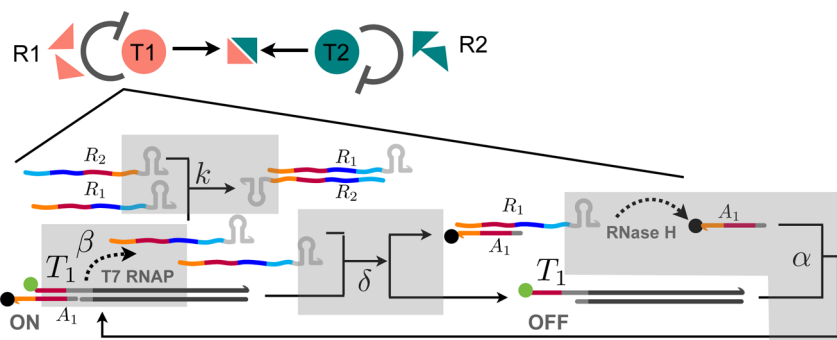


**Figure 5.** Summary scheme of DNA species and enzymes used to implement experimentally our negative feedback system for RNA production matching. Only subsystem 1 is represented (subsystem 2 is specular to subsystem 1). Complementary domains are indicated with the same color. RNA species  $R_1$  and  $R_2$ , transcribed by active genelets  $T_1$  and  $T_2$ , are designed to be complementary (dark red and dark blue domains), but also to function as self-inhibiting species. The orange-dark red domains in  $R_1$  indicate complementarity to the nicked portion of the promoter, activator  $A_1$ , which is displaced by free  $R_1$  (in excess with respect to  $R_2$ ) through toehold-mediated branch migration. The complex  $R_1 \cdot A_1$  is degraded by RNase H, which releases in solution  $A_1$ ; thus,  $A_1$  and  $T_1$  bind, recovering the genelet activity. Genelet activity can be tracked using a fluorophore-quencher pair (green and black dot positioned on  $T_1$  and  $A_1$ ). Gray boxes map the main pathways in this system to the simplified reactions of our model problem.

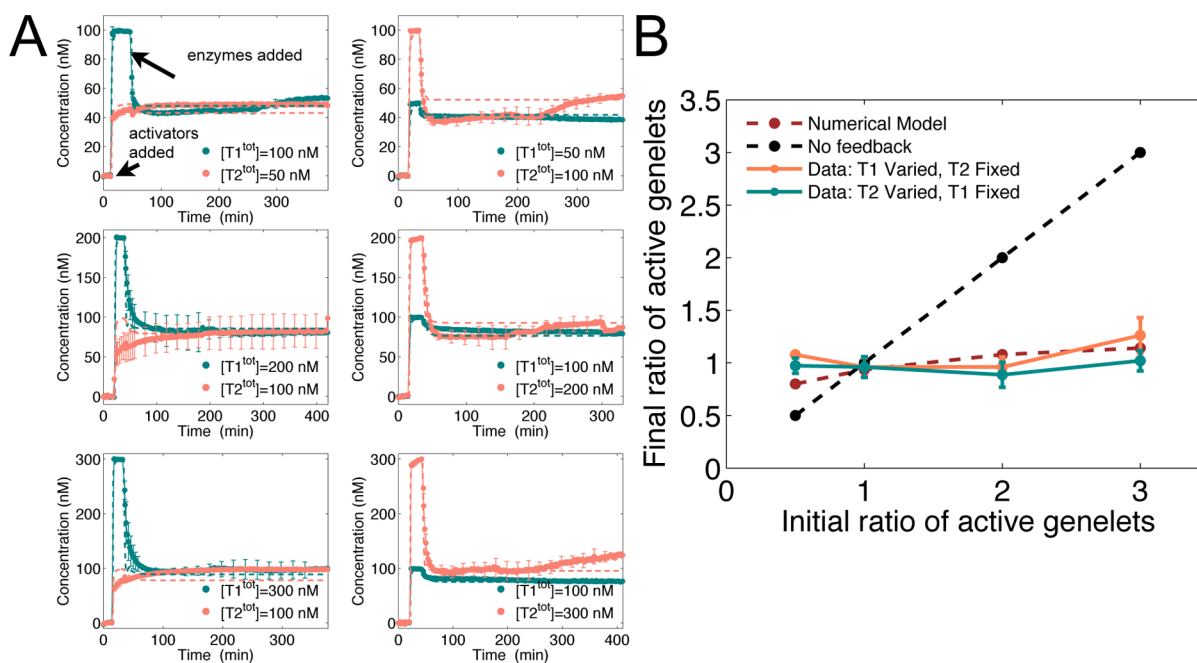


**Figure 6.** (A) Experimental fluorimetry data showing several time courses of our system, measured for different total concentrations of genelets. Experiments were run in triplicates. Error bars indicate the standard deviation at each time point. Once activators are added, both genelets become fully active. Addition of enzymes initiates production of  $R_1$  and  $R_2$ , which rapidly form a complex; excess of either species is expected to downregulate its own genelet activity. For example, in the top left panel  $[T_1^{\text{tot}}]$  is present in solution at a concentration which is twice that of  $[T_2^{\text{tot}}]$ : as expected, excess  $R_1$  inactivates  $T_1$  to activity levels comparable to  $[T_2^{\text{tot}}]$ . (B) This plot summarizes the behavior of the time courses at panel A, by showing the ratio of total genelet concentration ( $[T_i^{\text{tot}}]/[T_j^{\text{tot}}]$ , for  $i = 1, 2$  and  $j = 2, 1$ ) versus the steady state ratio of active genelet concentration ( $[T_i \cdot A_i]/[T_j \cdot A_j]$ , for  $i = 1, 2$  and  $j = 2, 1$ ). (The total concentration of activators is always identical to the concentration of templates.) In a wide range of conditions the steady state activity of the genelets always achieves a 1:1 ratio, thus matching production and demand of the RNA outputs.

again that flux matching is lost for low values of  $\delta$ . (The flux mismatch is averaged over the last hour of a 10 h trajectory simulation.)

**Experimental Results: Negative Autoregulation Balances RNA Transcription Rates in a Two-Gene Artificial Network.** We implemented experimentally the two-species model problem described above using *in vitro* transcriptional circuits.<sup>20</sup> A sketch of the reactions for subsystem 1 is in Figure 5, where we highlight the regulatory domains of nucleic acid species, the main chemical reactions occurring, and the simple model pathways to which they correspond. Two short, linear genetic switches, or genelets, correspond to species  $T_1$  and  $T_2$ , activated

by species  $A_1$  and  $A_2$ ; the genelets' outputs are the RNA transcripts  $R_1$  and  $R_2$ . Transcription is carried out by T7 RNA polymerase. The transcripts are designed to bind and form an inert RNA complex  $P = R_1 \cdot R_2$ . (Since the focus of this work is the investigation of the effects of feedback, the structure of  $P$  and its functionality as a stand alone complex are neglected.) Genelets have a nicked T7 bacteriophage promoter sequence that can be displaced by toehold-mediated branch migration.<sup>36</sup> We design the RNA output of each genelet to be complementary to the portion of the promoter that can be displaced (activator strand  $A_i$ ): therefore, free RNA in solution displaces the activator and self-inhibits its own production

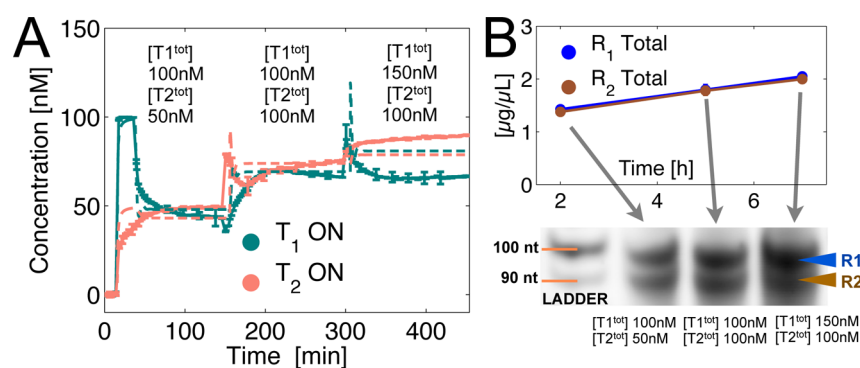


**Figure 7.** (A) We varied the total concentration of genelets over time, maintaining activators and templates stoichiometric. Experiments were run in triplicates. The system shows adaptation: when the concentration  $[T_2^{tot}]$  is increased to 100 nM, we observe an increase in the activity level for  $T_1$ , which was previously half-repressed. Further increase in the concentration  $[T_1^{tot}]$ , however, only marginally changes the activity levels, because the activity of  $T_2$  is nearly at maximal levels. (B) We sampled our time course experiments over time, and estimated the concentration of  $R_1$  and  $R_2$  through gel electrophoresis. The two concentrations remain comparable despite the changes in total genelet concentrations, further supporting our hypothesis that this negative feedback scheme matches production and demand by regulating genelet activity.

bringing the genelet in an “off” state. Degradation in the system is introduced by RNase H, which hydrolyzes RNA in DNA/RNA complexes. DNA strands were systematically designed by thermodynamic analysis using the Winfree lab DNA design toolbox for MATLAB, Nupack,<sup>27</sup> and Mfold.<sup>37</sup> Sequences were optimized to yield free energy gains favoring the desired reactions, and to avoid unwanted secondary structures and crosstalk. For example, we ensured that the  $R_1 \cdot R_2$  complex formation reaction be more favorable than the self-inhibition reaction: because roughly twice as many base-pairs are complementary in the  $R_1 \cdot R_2$  complex relative to the  $R_i \cdot A_i$  (inhibition) complex, the  $\Delta G$  of formation of  $R_1 \cdot R_2$  is  $\approx -110$  kcal/mol, twice as large (in absolute value) as the  $\Delta G$  of formation of  $R_i \cdot A_i$ , which is  $\approx -41$  kcal/mol. Strand sequences and complete reaction schematics are in section 1 of the SI.

We expect the feedback scheme to downregulate the production of either RNA species when in excess with respect to the other. For instance, if the concentration of genelet 1 is twice the concentration of genelet 2, in the absence of regulation the concentration of  $R_1$  produced will clearly exceed that of  $R_2$ . However, in the presence of negative feedback, we expect to observe downregulation of the active gene 1 to achieve concentrations close to the active concentration of gene 2. This expectation is quantitatively plausible, since the promoters used in both genelets are identical and their activity is thus similar. We can easily verify this hypothesis by labeling the 5' end of the nontemplate strand of each genelet with a fluorescent dye, and by labeling the corresponding activator strand with a quencher on the 3' end. Inactive templates will emit a high fluorescence signal, while the signal of active templates will be quenched (Figure 5, green and black dots respectively represent fluorophores and quenchers). For instance, when  $A_1$  is stripped off active  $T_1$ , the  $T_1$  fluorescence signal will increase. However, to improve the clarity of our plots, fluorescence traces reported here are processed to show a high measured signal in correspondence to a high genelet activity. In our experiments, the total amount of activators is stoichiometric to the total amount of templates; for brevity, we will just indicate the total concentration of  $T^{tot}$ , with the understanding that  $[A_i^{tot}] = [T_i^{tot}]$ .

Figure 6A shows the behavior of the system in the scenario described above, that is, when the total concentration of the two genelets is in a 2:1 ratio. As soon as enzymes are added in

solution and transcription is initiated, the formation of complex  $R_1 \cdot R_2$  is limited by the lower production rate of gene 2 (present in a lower amount). Thus, excess  $R_1$  reduces its own production by displacing its activator from the genelet, and balances the active concentration of the two genes to be practically identical. Thus, the steady state ratio of active genelets is close to one. Dashed lines in the figure are numerical traces generated by a detailed model comprised of several differential equations, whose parameters were fitted to the collected data.

We repeated this experiment for a variety of genelet ratios, keeping the concentration of one of the genelets constant and varying the concentration of the other gene. The steady state ratio of the active genelets was close to one in all cases (our complete data sets are in section 1.6 of the SI). Figure 6B summarizes this experimental assay and shows that our negative autoregulation scheme guarantees matched production and demand in a wide range of conditions. While we ran experiments exploring total genelet ratios up to 3:1, our detailed numerical model of the system predicts that the genelet activity is matched also for larger ratios (Figure S4 in the SI file shows that a matching activity ratio close to one is achieved for ratios of up to 10:1).

When the concentration of genelets varies over time, the negative feedback scheme handles a change in demand by automatically adapting the amount of each active genelet. Figure 7A shows that abrupt changes in the total concentration of one of the genelets are followed by an adjustment in the concentration of the excess species to guarantee a matched flux of the RNA products. We estimated the total amount of each RNA species produced during this experiment by gel electrophoresis, verifying that their production rate is adapted and their concentration is in a 1:1 stoichiometry.

**Mathematical Modeling.** We built a model for the *in vitro* two-gene flux matching system, starting from a complete list of reactions involving the nucleic acid and enzyme species. Using the law of mass action, we derived a set of ordinary differential equations (ODEs) which were numerically solved using MATLAB. The list of reactions (reported in section 2.2 of the SI) includes both the designed interactions among species, and some of the expected undesired reactions. Specifically, we include reactions of (weak) transcription for genelets in an off state. In addition, our design specifications result in an undesired binding domain between  $T_i$  and  $R_j$ , which is

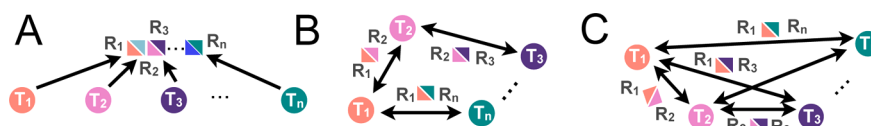


**Figure 8.** We explore the scalability of our two-device network by looking at three limit cases where  $n$  devices are interconnected through their binding outputs. (A) Single product interconnection. (B) Neighbor interconnection. (C) Handshake interconnection.

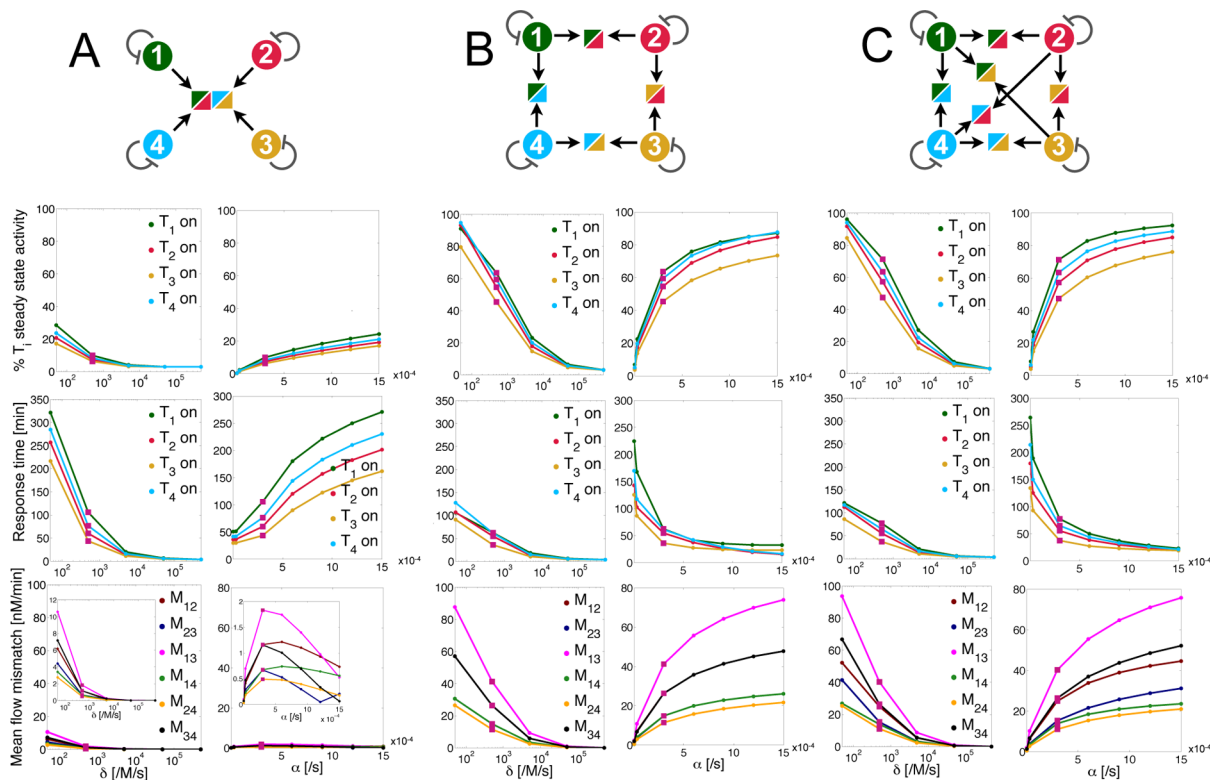


**Figure 9.** Sensitivity of  $T_i$  percent activity,  $T_i$  response time, and flux mismatch between pairs of outputs  $R_p$ , with respect to the negative feedback rate  $\delta$  and the spontaneous reactivation  $\alpha$ . (A) Single product interconnection. (B) Neighbor interconnection. (C) Handshake interconnection. Pink squares mark the system behavior in nominal conditions.

considered a further off state of the genelet. Such complex is a substrate for RNase H and the RNA strand is degraded by the enzyme, releasing the genelet activation domain. The transcription efficiency of an RNA-DNA promoter complex is very low.<sup>24</sup> We are aware of other sources of uncertainty when modeling genelet systems, including transcription bursting and RNA polymerase activity decay phenomena, abortive transcription, and partial RNase H mediated degradation of RNA-DNA hybrids: these phenomena result in the accumulation of short RNA species in the system that can be considered “waste” and may interfere with the desired dynamics. We found that these events play an important role in complex dynamical systems such as oscillators,<sup>23,24</sup> whose temporal behavior is highly sensitive to variations in the enzyme characteristics (which change from batch to batch) and notoriously difficult to model quantitatively. However, the experimental outcomes of our negative autoregulation system were satisfactorily captured by a detailed model that did not include the aforementioned phenomena. The deviation of our model predictions from the data measured in the adaptation experiments at Figure 7 are likely to be caused by the unmodeled accumulation of waste species in the system.

Our ODE model was simultaneously fitted to the fluorimetry data shown in Figure 6 and in Figure S2 of the SI file. The fitted

parameters were then used to predict the adaptive behavior of the system shown in Figure 7 and to explore the ability of the system to operate at total genelet ratios up to 10:1 (SI, Figure S4).

**Scalability and Alternative Architectures.** The size of synthetic biological circuits, from metabolic networks<sup>38</sup> to molecular computers,<sup>32,39</sup> is rapidly increasing to include hundreds of components. Thus, we ask if our negative feedback scheme is scalable to a larger number of interconnected modules. For instance, our two-gene circuit, where two RNA outputs interact to form a complex, could be extended to  $n$  genes whose outputs assemble in a single product. From a practical perspective, formation of cotranscriptional self-assembled RNA structures has been demonstrated<sup>6</sup> in the absence of any regulatory pathways for transcription; stoichiometric imbalances caused by transcriptional delay of long RNA strands were compensated by manually tuning the concentration of genes. The use of feedback could automatically tune the genes’ activity and regulate the stoichiometry of RNA components, thus improving the yield of correctly assembled structures.

We also ask if alternative feedback mechanisms can achieve production and demand matching in molecular devices. Positive feedback can easily generate instability in conventional

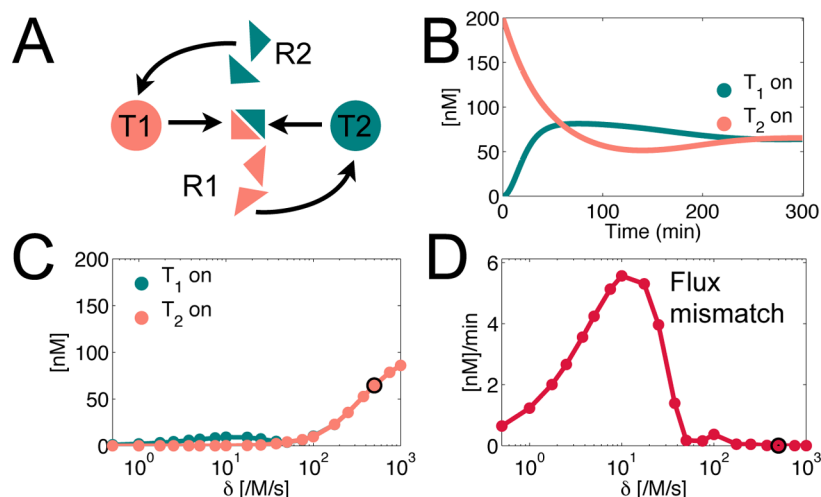


**Figure 10.** (A) Positive feedback architecture to match production and demand of interconnected devices. (B) Numerical simulation showing the time course of  $T_1$  and  $T_2$ . (C) Steady state activity of  $T_1$  and  $T_2$  as a function of the positive feedback parameter  $\delta$ . (D) Mismatch in the flux of  $R_1$  and  $R_2$  as a function of  $\delta$ . The dark circle in panels C and D marks the nominal conditions used for the time course plotted in panel B.

engineered systems and is thus carefully avoided by systems and control engineers. In contrast, positive feedback is commonly found in biology, in particular in gene networks<sup>10</sup> in the context of autoregulation<sup>11</sup> or within more complex motifs.<sup>40,41</sup> Motivated by Savageau's theory of positive autoregulation being common for proteins in high demand,<sup>11,12</sup> we consider an alternative architecture for matching production and demand that is based on cross activation.

**Scalability.** To investigate how the performance of negative autoregulation would scale in the context of a network composed by  $n$  molecular devices, we identified three canonical topologies for the output interactions. We say that two devices are interconnected if their outputs bind or assemble to form one or more products. Our two-gene network can immediately be scaled up to what we can call a "single product" topology (Figure 8A) with  $n$  participating species. When more than one assembled product is generated, we identify two limit cases: (1) the output of each device participates in at most two products, creating a "neighbor" topology (Figure 8B); (2) the output of each device participates in  $n - 1$  products, generating a "handshake" topology (Figure 8C). From an input/output perspective, we expect that the neighbor and handshake topologies can be rendered equivalent to the single product architecture, by designing appropriate downstream interactions among the network complexes. For example, complexes created by interacting pairs of outputs (neighbor topology) may further interact with one another and generate a single output assembly (single product).

We ask if, in all these possible topologies, our negative autoregulation scheme can still help modulate the activity of each device in order to match production and demand of each output. With numerical simulations we explored the behavior of up to four-component networks for each of the topologies described above. The simple model of ODEs (1)-(2) can be straightforwardly modified to model each topology, as reported in section 3.1 of the SI.

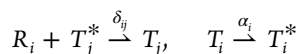
Simulation results show that negative feedback is still effective in regulating the devices activity: it reduces both steady state activity of  $T_i$  and the mean flow mismatch. The evolution over time of each species is very similar to the one shown in Figure 4A for the case of two molecular devices;

example time trajectories for  $n = 4$  are reported section 3.1 of the SI.

From a network design perspective, it is interesting to explore the performance of different interconnection topologies as a function of key parameters such as the feedback strength,  $\delta$ , and the rate of spontaneous gene activation,  $\alpha$ . For illustrative purposes, in Figure 9 we compare the performance of our three feedback topologies for  $n = 4$  within a range of values for  $\delta$  and  $\alpha$ . In each panel, a pink square marks the system behavior in nominal conditions,  $k_{ij} = 2 \times 10^3/\text{M}\cdot\text{s}$  for the handshake/neighbor topology,  $k = 6 \times 10^3/\text{M}\cdot\text{s}$  for the single product topology,  $\delta_i = 5 \times 10^3/\text{M}\cdot\text{s}$ ,  $\alpha_i = 3 \times 10^{-4}/\text{s}$ ,  $\beta_i = 1 \times 10^{-2}/\text{s}$ . An imbalance in the production rates of  $R_i$  is created by setting  $[T_i](0) = [T_i^{\text{tot}}]$ , while  $[R_i](0) = 0$ , choosing  $[T_1^{\text{tot}}] = 100$  nM,  $[T_2^{\text{tot}}] = 200$  nM,  $[T_3^{\text{tot}}] = 300$  nM,  $[T_4^{\text{tot}}] = 150$  nM. We report the percent steady state activity level of  $T_i$ , defined as  $[T_i]/[T_i^{\text{tot}}] \times 100$ , and the flux mismatch for each pair of outputs: each point in these graphs corresponds to the behavior of each subsystem averaged over the last hour (stationary behavior) of a 10 h numerical simulation. We also report the response time of  $T_i$ , computed as the time it takes for the active  $T_i$  trajectory to go from  $([T_i(0)] - 10\% \Delta)$  to  $([T_i(0)] - 90\% \Delta)$ , where  $\Delta$  is the difference between its initial value  $[T_i(0)]$  and its steady state value.

Referring to Figure 9, we can see that the steady state activity of  $T_i$  is higher for neighbor (Figure 9B) and handshake (Figure 9C) topologies; nevertheless, for all topologies the steady state activity of  $T_i$  decreases when  $\delta$  increases, and it increases when  $\alpha$  increases. The sensitivity of steady state  $T_i$  activity with respect to  $\alpha$  is lowest in the single product topology: this may be regarded as a benefit or a flaw of the system, depending on the downstream demand for the overall product complex ( $P = \Pi_i R_i$ ). The lowest flux mismatch is achieved in the single product topology (Figure 9A). However, for low values of negative feedback rate  $\delta$  this topology yields a much slower response time for  $T_i$ , relative to the neighbor and handshake structures. For large spontaneous gene activation rate  $\alpha$  the response time decreases in the neighbor/handshake topologies, but it increases in the single product topology. Thus, while the single product topology is more effective in matching production and demand of each output  $R_i$ , its response time is large relative to other topologies, and more sensitive to  $\alpha$ .

**Alternative Positive Feedback Architecture.** We explore numerically the performance of a two-device system where excess outputs cross-activate their production, rather than self-inhibit. This scheme is expected to increase the overall network output production rate, due to mutual activation of the generating species. Figure 10A shows a sketch of the system we consider. Two generating species  $T_1$  and  $T_2$  create outputs  $R_1$  and  $R_2$ , which bind to form a product  $P = R_1 \cdot R_2$ . Free molecules of  $R_i$ , not incorporated in  $P$ , generate a positive loop by binding to inactive  $T_j$  and activating it:



where again  $T_i^*$  is an inactive complex and  $[T_i^{\text{tot}}] = [T_i] + [T_i^*]$ . The total amount of  $R_i$  is  $[R_i^{\text{tot}}] = [R_i] + [T_j] + [P]$ . We now assume that  $T_i$  naturally reverts to its inactive state with rate  $\alpha_i$ . The corresponding differential equations are

$$\begin{aligned} \frac{d[T_i]}{dt} &= -\alpha_i[T_i] + \delta_{ji}[R_j]([T_i^{\text{tot}}] - [T_i]) \\ \frac{d[R_i]}{dt} &= \beta_i[T_i] - k[R_i][R_j] - \delta_{ij}[R_i]([T_j^{\text{tot}}] - [T_j]) \end{aligned} \quad (4)$$

The above differential equations were solved numerically. For illustrative purposes, our choice of parameters is consistent with the numerical study of the negative feedback circuit:  $\alpha_1 = \alpha_2 = 3 \times 10^{-4}$  /s,  $\beta_1 = \beta_2 = 0.01$ /s,  $\delta_1 = \delta_2 = 5 \times 10^2$ /M·s, and  $k = 2 \times 10^3$ /M·s. The total amount of templates was chosen as  $[T_1^{\text{tot}}] = 100$  nM,  $[T_2^{\text{tot}}] = 200$  nM. The initial conditions of active  $[T_i]$  are set as  $[T_1](0) = 0$  nM and  $[T_2](0) = 200$  nM, while  $[R_1](0) = [R_2](0) = 0$ . As a function of the positive feedback strength (for simplicity we picked  $\delta = \delta_1 = \delta_2$ ), the steady state amount of active  $T_i$  clearly increases (we define our steady state as the mean active  $[T_i]$  during the last one hour of a 10 h trajectory simulation), as shown in Figure 10C. We compute the flux of  $R_i$  again as the derivative of the total amount of  $[R_i^{\text{tot}}] = [R_i] + [R_i T_j] + [P]$ . The flux mismatch between  $R_1$  and  $R_2$  is defined again as the absolute value of the difference between the two fluxes; the average flux mismatch over the last hour of a 10-h simulation is plotted as a function of  $\delta$  in Figure 10D. Unlike the negative feedback architecture (cf. Figure 4D), the flux mismatch is not monotonically decreasing as a function of  $\delta$ ; however, a sufficiently large positive feedback yields matching fluxes and, as expected, higher activity levels relative to the negative feedback scheme (Figure 10C and D).

We examined the nullclines and derived flux matching conditions for the positive feedback architecture as done for the negative feedback scheme; the complete derivations are in section 4.1 of the SI. Again, we find that the circuit has, for a certain range of parameters, the ability to match the flux of outputs  $R_i$  by upregulating the production of output in lack. Because the production rate of  $R_i$  is limited by the finite maximal amount of activatable  $T_i$  (whose maximum active concentration equals  $[T_i^{\text{tot}}]$ ), the positive feedback loops cannot yield instability (*i.e.* uncontrolled increase) in the amount of unbound  $R_i$ . However, we observed that an overall upregulation of  $T_i$  activity results in slower response time for the circuit.

We explored the performance of the cross-activation scheme in the context of the larger-scale interconnection schemes considered in the previous section (Figure 8). First, we have to remark that a cross-activation scheme scales poorly with the number of devices in the network. The number of required

regulatory reactions  $n_{\text{reg}}$  is equal to the product of three factors: the number of devices  $n$ , the number  $n_p$  of complexes generated by each device, and the number  $n_r$  of reactions required to form each product ( $n_{\text{reg}} = n n_p n_r$ ). Thus,  $n(n-1)$  regulatory reactions are required in the single product and handshake topologies, while  $2n$  reactions are required in the neighbor topology. In contrast, the negative autoregulation scheme requires  $n$  regulatory reactions regardless of the chosen output interconnection topology. Nevertheless, we evaluated the performance of this scheme for a 3-device network, for which handshake and neighbor topologies coincide. In section 5.4 of the SI, we report a steady state analysis with respect to  $\delta$  and  $\alpha$  which mirrors the analysis done for the negative feedback architecture. We find that increasing the positive feedback rate  $\delta$  increases the percent activity of each  $T_i$  in all topologies; interestingly, for the handshake/neighbor topologies the flux mismatch is worsened with a large  $\delta$ . The response time for each  $T_i$  is generally large (above 30–50 min), and improves for large  $\alpha$  and  $\delta$ .

This positive feedback architecture may be implemented using transcriptional circuits as done for the negative feedback system. We propose a plausible design scheme in Section 4.2 of the SI, together with numerical simulations listing all the expected reactions. While plausible, this design suffers from undesired self-inhibition pathways unavoidable with the proposed design. Preliminary experiments on this system<sup>31</sup> (not reported in this manuscript) highlight the need for improved reaction mechanisms with tighter control over such undesired reactions.

## DISCUSSION

We have described the use of negative feedback as a mechanism to match production and demand in biochemical networks, and we provided an experimental demonstration of its effectiveness using a synthetic transcriptional system *in vitro*.<sup>20,23,24</sup> We identified “demand” as a target ligand or binding site that sequesters the output of a molecular device: in the context of our implementation, we considered artificial “genelets” whose RNA outputs bind to downstream target RNA species. In the absence of regulation, uncertainty in the demand or in the production rate of the molecular device output can cause imbalances between the concentration of available and consumed output. This imbalance can in turn result in accumulation of undesired reactants in a network, and result in malfunction of a device otherwise performing well in isolation. We show that negative autoregulation provides several advantages, in particular minimization of unused output of a device and robustness of its activity level relative to uncertainty in the output production rate. We also find that negative feedback helps reduce the sensitivity of the available output fraction with respect to uncertain downstream “load” (demand) concentration: these results are consistent with the role of negative feedback in retroactivity theory.<sup>34</sup> However, unlike the typical retroactivity theory setting, we consider a “consumptive” load binding mechanism (*i.e.* the load binds irreversibly to the output), and we do not include an output amplification “gain” as part of our feedback scheme. We note that the use of a transcriptional circuit to provide RNA “fuel” to a downstream DNA load was previously explored,<sup>42</sup> albeit without including an explicit feedback mechanism to autoregulate the RNA production rate; the mechanism of output/load interaction was subject to RNase H degradation

modeled with Michaelis–Menten dynamics, which provides implicit negative feedback.

The ability of negative feedback to automatically tune activity as a function of downstream demand is particularly relevant when the outputs of multiple devices interact to create possibly complex functionalities or assemblies. Uncertainty and variability of molecular demand would be significant challenges that careful open-loop tuning of each device would not address. We considered a minimal, two-elements network where the outputs interact to form a product, and excess of either output is designed to downregulate its own production. We designed a transcriptional network where the RNA transcripts of two synthetic genes are complementary and bind to form an inert product; however, excess of either RNA species self-inhibits by promoter displacement. Our assays show that, as expected, negative feedback balances production and demand in the synthetic genes, leveling their activity to comparable levels. Finally, through numerical analysis we examined the scalability of our system to networks of  $n$  devices, identifying three possible topologies of output interconnection. Negative autoregulation still guarantees a matched flux of outputs for all considered topologies. By comparing the performance of different interconnection schemes, we can see that topologies with a larger number of interconnections achieve faster response times; moreover, for these topologies, compared to single product interconnection, genelet steady state activity and relative flux mismatch are more easily tunable for each device as a function of the negative feedback reaction rates.

Through numerical simulations we contrasted negative autoregulation with a cross-activation scheme. Our analysis suggests that this positive feedback scheme is effective in matching and maximizing production rates within a network, and it would be thus appropriate for products in high demand.<sup>11</sup> However, its experimental implementation using transcriptional networks is challenging (as discussed in section 4.2 of the SI) due to the presence of undesired self-inhibitory interactions not easily avoidable by design; these unwanted reactions may be eliminated using “translator” DNA gates.<sup>43,44</sup> Again through simulations, we showed that our cross-activation scheme can achieve matched production and demand in larger networks, but the number of required regulatory pathways scales poorly with the number of devices. In addition, our analysis for networks with 2 and 3 interconnected devices highlights that positive feedback slows down the network response time (relative to a negative autoregulation-based network with consistent parameters). This observation agrees with the slow response time introduced by positive feedback in transcriptional control of gene expression,<sup>45</sup> and with the delay-inducing behavior of feedforward loops.<sup>45</sup>

Our experimental implementation using transcriptional circuits shows the viability of the negative autoregulation scheme in the context of *in vitro* networks.<sup>25</sup> Transcriptional circuits have been used as a toolbox to build a variety of devices including toggle switches,<sup>20</sup> memory elements,<sup>46</sup> oscillators,<sup>23,24</sup> and a variety of other network motifs.<sup>42,47</sup> These circuits are easily programmable and expandable: regulatory interactions are designed through nucleic acid strand displacement and hybridization cascades, whose thermodynamics and kinetics can be predictably tuned by optimizing their base pair content<sup>48</sup> with a variety of software toolboxes.<sup>26,27</sup> Rationally programmed nucleic acid networks can be easily interfaced with an array of ligands and physical signals through aptamers.<sup>49,50</sup> Thus, the significance of our experimental implementation goes

beyond the proof of a principle: systematic use of negative autoregulation in the context of complex synthetic *in vitro* DNA networks will improve their robustness and adaptability to uncertainty in the environment. In particular, our scheme may be immediately used in the context of regulated, cotranscriptional production of RNA self-assembled structures,<sup>6,7</sup> where mismatched production and demand of components can favor the formation of incorrect complexes.

The bottom-up construction of dynamic molecular devices is a tremendous opportunity to both improve our understanding of natural biological functions and create new, artificial biotechnologies. Negative feedback has been widely used to design and tune the dynamics of synthetic *in vitro* devices such as oscillators and bistable systems.<sup>20,23,24,51,52</sup> We envision that negative feedback will also be needed to guarantee functionality when multiple devices are integrated in large scale networks, possibly requiring hierarchical, layered feedback loops akin to modern networked control systems.<sup>8</sup> Negative autoregulation mechanisms similar to the architecture described in this work will be useful not only to automatically match production and demand of individual biochemical production processes,<sup>53,54</sup> but also to guarantee modular and adaptive input-output behaviors of components within a complex interconnected system.

#### 4. METHODS

**DNA Oligonucleotides and Enzymes.** All the strands were purchased from Integrated DNA Technologies, Coralville, IA. Genelets were labeled with TAMRA and Texas Red at the 5' and of their nontemplate strands; activators were labeled with the IOWA black RQ quencher at the 3' end. For transcription experiments we used the T7Megashortscript kit (#1354), Ambion, Austin, TX, which includes a proprietary T7 RNA polymerase enzyme mix. *E. coli* RNase H was purchased from Ambion (#2292).

**Oligonucleotide Sequences.** Sequences are reported in section 1.2 of the SI file.

**Transcription.** Genelet templates were annealed with 10% (v/v) 10× transcription buffer—part of the T7Megashortscript kit (#1354)—from 90 to 37 °C for 1 h 30 min at a concentration 5–10× the target concentration. The DNA activators were added to the annealed templates from a higher concentration stock, in a solution with 10% (v/v), 10× transcription buffer, 7.5 mM each NTP, 4% (v/v) T7 RNA polymerase, and 0.44% (v/v) *E. coli* RNase H. Each transcription experiment for fluorescence spectroscopy was prepared for a total target volume of 70  $\mu$ L. Samples for gel studies were quenched using a denaturing dye (80% formamide, 10 mM EDTA, 0.01 g XCFE).

**Data Acquisition.** Fluorescence was measured at 37 °C every two minutes with a Horiba/Jobin Yvon Fluorolog 3 system. Excitation and emission maxima for TAMRA were set to 559 and 583 nm, respectively, according to the IDT recommendation; for Texas Red the maxima for the spectrum were set to 598–617 nm. Raw fluorescence data  $\Phi(t)$  were converted to estimated switch activity by normalizing with respect to maximum fluorescence  $\Phi_{\max}$  (measured before adding activators and enzymes) and to minimum fluorescence  $\Phi_{\min}$  (measured after adding activators and before adding enzymes):

$$[T_i A_i](t) = [T_i^{\text{tot}}] \left( 1 - \frac{\Phi(t) - \Phi_{\min}}{\Phi_{\max} - \Phi_{\min}} \right)$$

For the adaptation experiments, normalization was done by measuring maximum and minimum fluorescence levels at the beginning of the experiment, and assuming that the maximum fluorescence level scales linearly with the change in total fluorescently labeled strands, while the minimum is not significantly affected by that variation. We used the formula:

$$[T_i A_i](t) = \alpha [T_i^{\text{tot}}] \left( 1 - \frac{\Phi(t) - \Phi_{\min}}{\alpha \Phi_{\max} - \Phi_{\min}} \right)$$

where  $\alpha$  is a factor that scales the total amount of template as it varies in the experiment.

Denaturing polyacrylamide gels (8% 19:1 acrylamide:bis and 7 M urea in TBE buffer, 100 mM Tris, 90 mM boric acid, 1 mM EDTA) were run at 67 °C for 45 min with 10 V/cm in TBE buffer. Samples were loaded using Xylene Cyanol FF dye. For quantitation, denaturing gels were stained with SYBR Gold (Molecular Probes, Eugene, OR; #S-11494). As a reference, we used a 10-base DNA ladder (Invitrogen, Carlsbad, CA; #1082-015). Gels were scanned using the Molecular Imager FX (Biorad, Hercules, CA) and analyzed using the Quantity One software (Biorad, Hercules, CA).

**Numerical Simulations.** Numerical simulations were run using MATLAB (The MathWorks). Ordinary differential equations were integrated using the ode23 routine. Data fitting was performed using the fmincon routine. Details on the data fitting procedure are in section 1.6.4 of the SI.

## ■ ASSOCIATED CONTENT

### 📄 Supporting Information

Detailed information on materials, experimental methods, numerical simulations and additional references. This material is available free of charge *via* the Internet at <http://pubs.acs.org>.

## ■ AUTHOR INFORMATION

### Corresponding Author

\*E-mail: [efranco@engr.ucr.edu](mailto:efranco@engr.ucr.edu).

### Notes

The authors declare no competing financial interest.

## ■ ACKNOWLEDGMENTS

The authors thank Jongmin Kim, Paul W. K. Rothmund, Franco Blanchini, and Erik Winfree for their feedback. In particular, we thank Erik Winfree for sharing laboratory facilities. This work has been supported by the National Science Foundation through grants CCF-0832824 (“The Molecular Programming Project”) and CMMI-1266402, and by the Institute for Collaborative Biotechnologies through grant W911NF-09-0001 from the U.S. Army Research Office.

## ■ REFERENCES

- (1) Purnick, P. E., and Weiss, R. (2009) The second wave of synthetic biology: From modules to systems. *Nat. Rev. Mol. Cell Biol.* 10, 410–422.
- (2) Dong, H., Nilsson, L., and Kurland, C. G. (1995) Gratuitous overexpression of genes in *Escherichia coli* leads to growth inhibition and ribosome destruction. *J. Bacteriol.* 177, 1497–1504.
- (3) Scott, M., Gunderson, C. W., Mateescu, E. M., Zhang, Z., and Hwa, T. (2010) Interdependence of cell growth and gene expression: Origins and consequences. *Science* 330, 1099–1102.

- (4) Dunlop, M. J. (2011) Engineering microbes for tolerance to next-generation biofuels. *Biotechnol. Biofuels* 4, 32.

- (5) Pitera, D. J., Paddon, C. J., Newman, J. D., and Keasling, J. D. (2007) Balancing a heterologous mevalonate pathway for improved isoprenoid production in *Escherichia coli*. *Metab. Eng.* 9, 193–207.

- (6) Afonin, K. A., Bindewald, E., Yaghoubian, A. J., Voss, N., Jacovetty, E., Shapiro, B. A., and Jaeger, L. (2010) *In vitro* assembly of cubic RNA-based scaffolds designed *in silico*. *Nat. Nanotechnol.* 5, 676–682.

- (7) Delebecque, C. J., Lindner, A. B., Silver, P. A., and Aldaye, F. A. (2011) Organization of intracellular reactions with rationally designed RNA assemblies. *Science* 333, 470–474.

- (8) Åström, K. J. and Murray, R. (2010) *Feedback Systems: An Introduction for Scientists and Engineers*, Princeton University Press, Princeton, NJ.

- (9) Shen-Orr, S. S., Milo, R., Mangan, S., and Alon, U. (2002) Network motifs in the transcriptional regulation network of *Escherichia coli*. *Nat. Genet.* 31, 64–68.

- (10) Alon, U. (2007) *An Introduction to Systems Biology: Design Principles of Biological Circuits*, Chapman & Hall/CRC, Boca Raton, FL.

- (11) Savageau, M. A. (1977) Design of molecular control mechanisms and the demand for gene expression. *Proc. Natl. Acad. Sci.* 74, 5647–5651.

- (12) Shinar, G., Dekel, E., Tlusty, T., and Alon, U. (2006) Rules for biological regulation based on error minimization. *Nature* 103, 3999–4004.

- (13) Becskei, A., and Serrano, L. (2000) Engineering stability in gene networks by autoregulation. *Nature* 405, 590–593.

- (14) Austin, D., Allen, M., McCollum, J., Dar, R., Wilgus, J., Sayler, G., Samatova, N., Cox, C., and Simpson, M. (2006) Gene network shaping of inherent noise spectra. *Nature* 439, 608–611.

- (15) Nevozhay, D., Adams, R. M., Murphy, K. F., Josić, K., and Balázsi, G. (2009) Negative autoregulation linearizes the dose–response and suppresses the heterogeneity of gene expression. *Proc. Natl. Acad. Sci.* 106, 5123–5128.

- (16) Denby, C. M., Im, J. H., Richard, C. Y., Pesce, C. G., and Brem, R. B. (2012) Negative feedback confers mutational robustness in yeast transcription factor regulation. *Proc. Natl. Acad. Sci.* 109, 3874–3878.

- (17) Rosenfeld, N., Elowitz, M. B., and Alon, U. (2002) Negative autoregulation speeds the response times of transcription networks. *J. Mol. Biol.* 323, 785–793.

- (18) Deans, T. L., Cantor, C. R., and Collins, J. J. (2007) A tunable genetic switch based on RNAi and repressor proteins for regulating gene expression in mammalian cells. *Cell* 130, 363–372.

- (19) Shimoga, V., White, J. T., Li, Y., Sontag, E., and Bleris, L. (2013) Synthetic mammalian transgene negative autoregulation. *Mol. Syst. Biol.* 9, 1.

- (20) Kim, J., White, K. S., and Winfree, E. (2006) Construction of an *in vitro* bistable circuit from synthetic transcriptional switches. *Mol. Syst. Biol.* 1, 68.

- (21) Karig, D. K., Iyer, S., Simpson, M. L., and Doktycz, M. J. (2012) Expression optimization and synthetic gene networks in cell-free systems. *Nucleic Acids Res.* 40, 3763–3774.

- (22) Mori, Y., Nakamura, Y., and Ohuchi, S. (2012) Inhibitory RNA aptamer against SP6 RNA polymerase. *Biochem. Biophys. Res. Commun.* 420, 440–443.

- (23) Kim, J., and Winfree, E. (2011) Synthetic *in vitro* transcriptional oscillators. *Mol. Syst. Biol.* 7, 465.

- (24) Franco, E., Friedrichs, E., Kim, J., Jungmann, R., Murray, R., Winfree, E., and Simmel, F. C. (2011) Timing molecular motion and production with a synthetic transcriptional clock. *Proc. Natl. Acad. Sci.* 108, E784–E793.

- (25) Hockenberry, A. J., and Jewett, M. C. (2012) Synthetic *in vitro* circuits. *Curr. Opin. Chem. Biol.* 16, 253–259.

- (26) Markham, N. R., and Zuker, M. (2008) UNAFold software for nucleic acid folding and hybridization. *Methods Mol. Biol.* 453, 3–31.

- (27) Zadeh, J. N., Steenberg, C. D., Bois, J. S., Wolfe, B. R., Pierce, M. B., Khan, A. R., Dirks, R. M., and Pierce, N. A. (2011) NUPACK: Analysis of nucleic acid systems. *J. Comput. Chem.* 32, 170–173.
- (28) Franco, E., Forsberg, P.-O., and Murray, R. M. (2008) Design, modeling and synthesis of an *in vitro* transcription rate regulatory circuit. *American Control Conference, 2008*, 2786–2791, DOI: 10.1109/ACC.2008.4586915.
- (29) Franco, E., and Murray, R. M. (2008) Design and performance of *in vitro* transcription rate regulatory circuits. *47th IEEE Conference on Decision and Control*, 161–166.
- (30) Giordano, G., Franco, E., and Murray, R. M. (2013) Feedback architectures to regulate flux of components in artificial gene networks. *American Control Conference, 4747–4752*.
- (31) Franco, E. (2012) Analysis, design, and *in vitro* implementation of robust biochemical networks. Ph.D. thesis, California Institute of Technology.
- (32) Qian, L., and Winfree, E. (2011) Scaling up digital circuit computation with DNA strand displacement cascades. *Science* 3, 1196–1201.
- (33) Zhang, D. Y., Hariadi, R. F., Choi, H. M., and Winfree, E. (2013) Integrating DNA strand-displacement circuitry with DNA tile self-assembly. *Nat. Commun.* 4, 1965.
- (34) Del Vecchio, D., Ninfa, A., and Sontag, E. (2008) Modular cell biology: Retroactivity and insulation. *Mol. Syst. Biol.* 4, 161.
- (35) Bonacci, W., Teng, P. K., Afonso, B., Niederholtmeyer, H., Grob, P., Silver, P. A., and Savage, D. F. (2012) Modularity of a carbon-fixing protein organelle. *Proc. Natl. Acad. Sci.* 109, 478–483.
- (36) Yurke, B., and Mills, A. P. (2003) Using DNA to power nanostructures. *Genetic Programming and Evolvable Machines* 4, 111–122.
- (37) Zuker, M., and Stiegler, P. (1981) Optimal computer folding of large RNA sequences using thermodynamics and auxiliary information. *Nucleic Acids Res.* 9, 133–148.
- (38) Lee, S. K., Chou, H., Ham, T. S., Lee, T. S., and Keasling, J. D. (2008) Metabolic engineering of microorganisms for biofuels production: From bugs to synthetic biology to fuels. *Curr. Opin. Biotechnol.* 19, 556–563.
- (39) Xie, Z., Liu, S. J., Bleris, L., and Benenson, Y. (2010) Logic integration of mRNA signals by an RNAi-based molecular computer. *Nucleic Acids Res.* 38, 2692–2701.
- (40) Kaplan, S., Bren, A., Dekel, E., and Alon, U. (2008) The incoherent feed-forward loop can generate non-monotonic input functions for genes. *Mol. Syst. Biol.* 4, 1.
- (41) Mangan, S., Zaslaver, A., and Alon, U. (2003) The coherent feedforward loop serves as a sign-sensitive delay element in transcription networks. *J. Mol. Biol.* 334, 197–204.
- (42) Bishop, J. D., and Klavins, E. (2012) Characterization of a biomolecular fuel delivery device under load. *51st IEEE Conference on Decision and Control*, 3589–3594.
- (43) Soloveichik, D., Seelig, G., and Winfree, E. (2010) DNA as a universal substrate for chemical kinetics. *Proc. Natl. Acad. Sci.* 107, 5393–5398.
- (44) Chen, Y.-J., Dalchau, N., Srinivas, N., Phillips, A., Cardelli, L., Soloveichik, D., and Seelig, G. (2013) Programmable chemical controllers made from DNA. *Nat. Nanotechnol.* 8, 755–762.
- (45) Alon, U. (2007) Network motifs: theory and experimental approaches. *Nat. Rev. Genet.* 8, 450–461.
- (46) Subsoontorn, P., Kim, J., and Winfree, E. (2012) Ensemble Bayesian analysis of bistability in a synthetic transcriptional switch. *ACS Synth. Biol.* 1, 299–316.
- (47) Kim, J., and Murray, R. M. (2011) Analysis and design of a synthetic transcriptional network for exact adaptation. *IEEE Biomedical Circuits and Systems Conference (BioCAS)*, 345–348.
- (48) Zhang, D. Y., and Seelig, G. (2011) Dynamic DNA nanotechnology using strand-displacement reactions. *Nature Chem.* 3, 103–113.
- (49) Stoltenburg, R., Reinemann, C., and Strehlitz, B. (2007) SELEX—A (r)evolutionary method to generate high-affinity nucleic acid ligands. *Biomol. Eng.* 24, 381–403.
- (50) Ellington, A. D., and Szostak, J. W. (1990) *In vitro* selection of RNA molecules that bind specific ligands. *Nature* 346, 818–822.
- (51) Montagne, K., Plasson, R., Sakai, Y., Fujii, T., and Rondelez, Y. (2011) Programming an *in vitro* DNA oscillator using a molecular networking strategy. *Mol. Syst. Biol.* 7, 1.
- (52) Weitz, M., Kim, J., Kapsner, K., Winfree, E., Franco, E., and Simmel, F. C. (2014) Diversity in the dynamical behaviour of a compartmentalized programmable biochemical oscillator. *Nat. Chem.*, DOI: 10.1038/nchem.1869.
- (53) Hsiao, V., de los Santos, E. L., Whitaker, W. R., Dueber, J. E., and Murray, R. M. (2013) Design and implementation of a synthetic biomolecular concentration tracker. *bioRxiv*, DOI: 10.1101/000448.
- (54) de los Santos, E., Hsiao, V., and Murray, R. (2013) Design and implementation of a biomolecular circuit for tracking protein concentration. *American Control Conference*, 2290–2294.

# Negative autoregulation matches production and demand in synthetic transcriptional networks

Experimental methods, data processing, and modeling

Elisa Franco<sup>1,\*</sup>, Giulia Giordano<sup>2</sup>, Per-Ola Forsberg<sup>3</sup>, and Richard M. Murray<sup>4</sup>

<sup>1</sup>*Mechanical Engineering, University of California at Riverside, Riverside, CA 92521*

<sup>2</sup>*Department of Mathematics and Computer Science, University of Udine, Italy*

<sup>3</sup>*Kristianstad Central Hospital, 29832 Tollarp, Sweden*

<sup>4</sup>*Engineering and Applied Science, California Institute of Technology, Pasadena, CA 91125*

*\*Corresponding author*

# Contents

<b>1</b>	<b>Experimental implementation of a two-gene flux matching system based on negative autoregulation: Materials and methods</b>	<b>3</b>
1.1	Reactions and domains design . . . . .	3
1.2	Oligonucleotide sequences . . . . .	3
1.3	DNA oligonucleotides and enzymes . . . . .	5
1.4	Transcription protocol . . . . .	5
1.5	Data acquisition and processing . . . . .	5
1.6	Characterization assays . . . . .	6
1.6.1	Genelets in isolation . . . . .	6
1.6.2	Interconnected genelets . . . . .	6
1.6.3	Flux adaptation . . . . .	8
1.6.4	Data fitting . . . . .	8
<b>2</b>	<b>Modeling and numerical analysis: two-gene flux matching system</b>	<b>10</b>
2.1	Simple model system: derivation of nullclines and rate matching conditions . . .	10
2.2	Differential equations modeling the experimental implementation . . . . .	14
<b>3</b>	<b>Modeling and numerical analysis: Scalability of the negative feedback scheme for flux regulation</b>	<b>20</b>
3.1	Simple model system . . . . .	20
3.1.1	Single product topology . . . . .	20
3.1.2	Handshake and neighbor topologies . . . . .	22
3.1.3	Parameters . . . . .	22
3.1.4	Performance overview of the different topologies as a function of key parameters . . . . .	22
<b>4</b>	<b>Positive feedback architecture for a two-gene system. Modeling and a viable experimental implementation</b>	<b>26</b>
4.1	Simple model system: derivation of nullclines and rate matching conditions . . .	26
4.2	A possible experimental implementation of a two-gene positive feedback scheme	28
4.2.1	Modeling . . . . .	30
<b>5</b>	<b>Numerical scalability analysis of our simplified positive feedback scheme model for flux regulation</b>	<b>33</b>
5.1	Single product topology . . . . .	34
5.2	Handshake and neighbor topologies . . . . .	35
5.3	Parameters . . . . .	35
5.4	Performance overview of the different topologies as a function of key parameters	35

# 1 Experimental implementation of a two-gene flux matching system based on negative autoregulation: Materials and methods

## 1.1 Reactions and domains design

A graphical sketch of the domain-level design for the self-repression interconnection is shown in Figure S1 A. The RNA outputs of each genelet are designed so that:

- 1) Each RNA output has a domain complementary to its activator strand.
- 2) The two RNA species are also complementary.

These specifications introduce a binding domain between  $T_i$  and  $R_j$ , which is considered another off state, as shown in Figure S1 B. Such a complex is a substrate for RNase H and the RNA strand is degraded by the enzyme, releasing the genelet activation domain. We assume that the transcription efficiency of an RNA-DNA promoter complex is very low. This hypothesis was not experimentally challenged for this specific system; however data shown in Franco et al. [2011], Supplementary Information, show that this assumption is valid for other genelets with the same promoter domain.

The design of a self-inhibiting genelet was first characterized in Kim [2007]. The circuit design proposed here, with two-domain RNA transcripts, was originally presented in Franco et al. [2008].

DNA strands were designed by thermodynamic analysis using the Winfree lab DNA design toolbox for MATLAB, Nupack Zadeh et al. [2011] and Mfold Zuker and Stiegler [1981]. The strands were optimized to yield free energy gains favoring the desired reactions, and to avoid unwanted secondary structures and crosstalk. Further constraints on the length and structure of the strands, which can affect the transcription efficiency and fidelity, were taken into account referring to Kim [2007], Chapter 3.4.

## 1.2 Oligonucleotide sequences

Due to technical constraints of the supplier IDT DNA,  $T_1 - nt$  and  $T_2 - nt$  were shortened with respect to the nominal design to have a length of 125 bases. The strands used in the experiments are those denoted below as "Short". These modifications did not alter the regulatory domains of the transcripts  $R_1$  and  $R_2$ . Also the full length of the main transcription products was not affected, as verified by gel electrophoresis in Figure S2 B.

**T<sub>1</sub>-nt** Full (134-mer) 5'-CTA ATG AAC TAC TAC TAC ACA CTA ATA CGA CTC ACT ATA GGG AGA AAC AAG AAC GAC ACT AAT GAA CTA CTA CTA CAC ACC AAC CAC AAC TTT ACC TTA ACC TTA CTT ACC ACG GCA GCT GAC AAA GTC AGA AA-3' (not synthesized)

**T<sub>1</sub>-nt** Short (125-mer) 5'-Tamra-CT AAT GAA CTA CTA CTA CAC ACT AAT ACG ACT CAC TAT AGG GAG AAA CAA GAA CGA CAC TAA TGA ACT ACT ACT ACA CAC CAA CCA CAA CTT TAC CTT AAC CTT ACT TAC CAC GGC AGC TGA CAA-3'

**T<sub>1</sub>-t** (107-mer) 5'-TTT CTG ACT TTG TCA GCT GCC GTG GTA AGT AAG GTT AAG GTA AAG TTG TGG TTG GTG TGT AGT AGT AGT TCA TTA GTG TCG TTC TTG TTT CTC CCT ATA GTG AGT CG-3'

**A<sub>1</sub>** (35-mer) 5'-TAT TAG TGT GTA GTA GTA GTT CAT TAG TGT CGT TC-3'

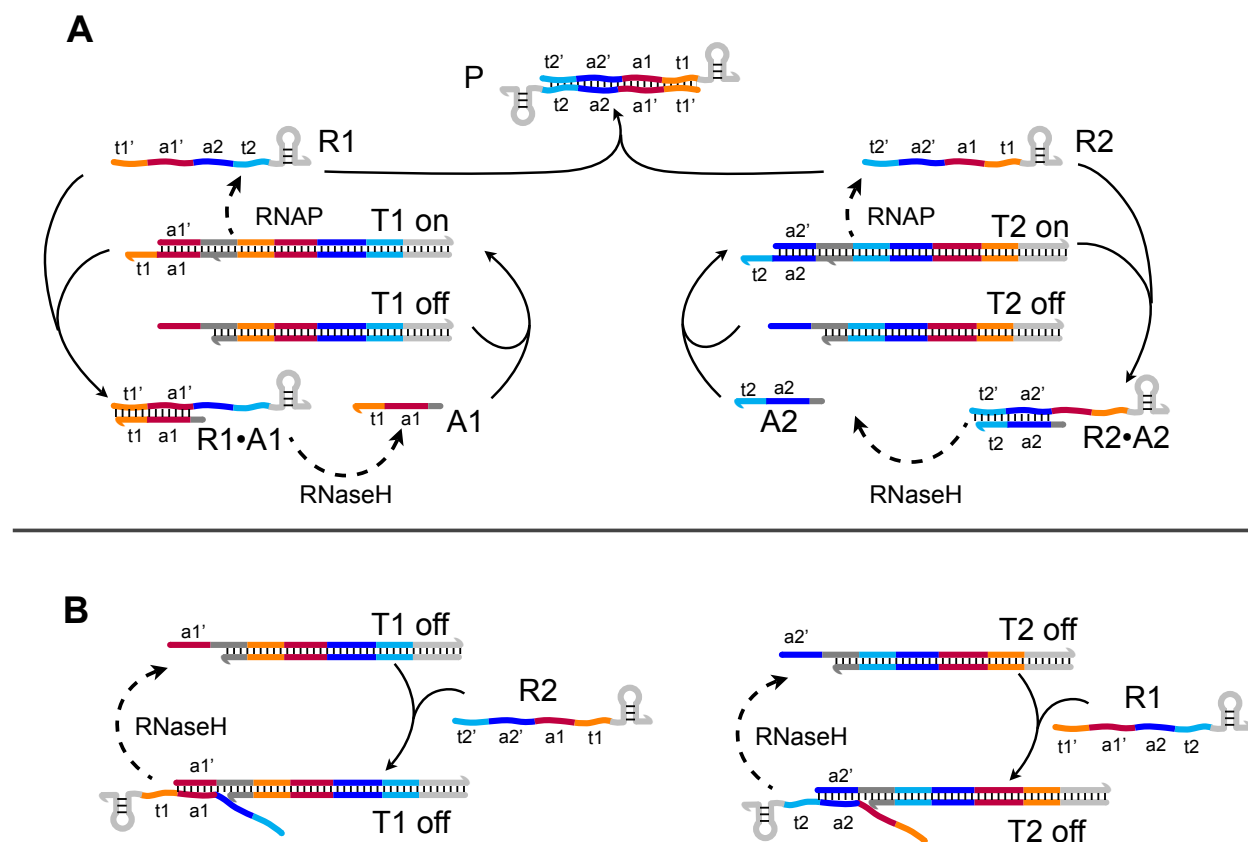


Figure S1: General reaction scheme representing a transcriptional circuit implementation of the two-gene negative feedback scheme for flux matching. Complementary domains have the same color. Promoters are in dark gray, terminator hairpin sequences in light gray. The RNA output of each genelet is designed to be complementary to its corresponding activator strand. The two RNA species are also complementary. A. Desired self-inhibition loops. B. Undesired cross-hybridization and RNase H mediated degradation of the RNA-template complexes.

**T<sub>2</sub>-nt** Full (126-mer) 5'-GGT TAA GGT AAA GTT GTG GTT GTA ATA CGA CTC ACT ATA GGG AGA AAC AAG TAA GTA AGG TTA AGG TAA AGT TGT GGT TGG TGT GTA GTA GTA GTT CAT TAG TGT CGT TCC TGA CAA AGT CAG AAA-3' (not synthesized)

**T<sub>2</sub>-nt** Short (126-mer) 5'-TexasRed-GG TTA AGG TAA AGT TGT GGT TGT AAT ACG ACT CAC TAT AGG GAG AAA CAA GTA AGT AAG GTT AAG GTA AAG TTG TGG TTG GTG TGT AGT AGT AGT TCA TTA GTG TCG TTC CTG ACA AAG TCA GAA-3'

**T<sub>2</sub>-t** (99-mer) 5'-TTT CTG ACT TTG TCA GGA ACG ACA CTA ATG AAC TAC TAC TAC ACA CCA ACC ACA ACT TTA CCT TAA CCT TAC TTA CTT GTT TCT CCC TAT AGT GAG TCG-3'

**A<sub>2</sub>** (35-mer) 5'-TAT TAC AAC CAC AAC TTT ACC TTA ACC TTA CTT AC-3'

**R<sub>1</sub>** (95-mer) 5' - GGG AGA AAC AAG AAC GAC ACU AAU GAA CUA CUA CUA CAC ACC AAC CAC AAC UUU ACC UUA ACC UUA CUU ACC ACG GCA GCU GAC AAA GUC AGA AA -3'

**R<sub>2</sub>** (87-mer) 5'-GGG AGA AAC AAG UAA GUA AGG UUA AGG UAA AGU UGU GGU UGG UGU GUA GUA GUA GUU CAU UAG UGU CGU UCC UGA CAA AGU CAG AAA -3'

### 1.3 DNA oligonucleotides and enzymes

All the strands were purchased from Integrated DNA Technologies, Coralville, IA IDT.  $T_1 - nt$  is labeled with TAMRA at the 5' end,  $T_2 - nt$  is labeled with Texas Red at the 5' end, both activators  $A_1$  and  $A_2$  are labeled with the IOWA black RQ quencher at the 3' end. The transcription buffer mix was prepared prior to each experiment run (two to four samples) using the T7 Megashortscript kit (#1354), Ambion, Austin, TX which includes the T7 RNA polymerase enzyme mix, the transcription buffer, and rNTPs utilized in the experiments. *E. coli* RNase H was purchased from Ambion (#2292).

### 1.4 Transcription protocol

The templates were annealed with 10% (v/v) 10× transcription buffer from 90°C to 37°C for 1 h 30 min at a concentration 5–10× the target concentration. The DNA activators were added to the annealed templates from a higher concentration stock, in a solution with 10% (v/v), 10× transcription buffer, 7.5 mM each NTP, 4% (v/v) T7 RNA polymerase, and .44% (v/v) *E. coli* RNase H. Each transcription experiment for fluorescence spectroscopy was prepared for a total target volume of 70  $\mu$ l. Samples for gel studies were quenched using a denaturing dye (80% formamide, 10 mM EDTA, 0.01g XCFF).

### 1.5 Data acquisition and processing

The fluorescence was measured at 37°C every two minutes with a Horiba/Jobin Yvon Fluorolog 3 system. Excitation and emission maxima for TAMRA were set to 559 nm and 583 nm, respectively, according to the IDT recommendation; for Texas Red the maxima for the spectrum were set to 598–617 nm. Slit widths were set to 2 nM for excitation and 4 nM for emission. The raw fluorescence data  $\Phi(t)$  were converted to estimated switch activity by normalizing with respect to maximum fluorescence  $\Phi_{\max}$  (measured before adding activators and enzymes) and to minimum

fluorescence  $\Phi_{\min}$  (measured after adding activators and before adding enzymes):

$$[T_i A_i](t) = [T_i^{tot}] \cdot \left( 1 - \frac{\Phi(t) - \Phi_{\min}}{\Phi_{\max} - \Phi_{\min}} \right).$$

For the adaptation experiments, normalization was done by measuring maximum and minimum fluorescence levels at the beginning of the experiment, and assuming that the maximum fluorescence level scales linearly with the change in total fluorescently labeled strands, while the minimum is not significantly affected by that variation. We used the formula:

$$[T_i A_i](t) = \alpha [T_i^{tot}] \cdot \left( 1 - \frac{\Phi(t) - \Phi_{\min}}{\alpha \Phi_{\max} - \Phi_{\min}} \right),$$

where  $\alpha$  is a factor that scales the total amount of template as it varies in the experiment.

Denaturing polyacrylamide gels (8% 19:1 acrylamide:bis and 7 M urea in TBE buffer, 100 mM Tris, 90 mM boric acid, 1 mM EDTA) were run at 67°C for 45 min with 10 V/cm in TBE buffer. Samples were loaded using Xylene Cyanol FF dye. For quantitation, denaturing gels were stained with SYBR Gold (Molecular Probes, Eugene, OR; #S-11494). In the control lane a 10-base DNA ladder (Invitrogen, Carlsbad, CA; #1082-015) was utilized. The DNA ladder 100 bp band was used as a control to roughly estimate the concentrations of the RNA species in solution in Figure S5 E and F. Gels were scanned using the Molecular Imager FX (Biorad, Hercules, CA) and analyzed using the Quantity One software (Biorad, Hercules, CA).

## 1.6 Characterization assays

This section reports experimental results and numerical fits. All experiments were run in triplicates: mean and error bars (standard deviation) are shown in each figure, together with the simulated traces (dashed lines) from our fitted model. The full derivation for the model fitted to the data is in Section 2.2.

### 1.6.1 Genelets in isolation

Figure S2 A shows the behavior of the two genelets in isolation: we can verify that each genelet self-inhibits after the enzymes are added. (For details on the data normalization procedure, refer to Section 1.5.) The concentration of RNA present in solution can be measured through gel electrophoresis, as shown in Figure S2 B: lanes 1 and 2 show that free RNA in solution is effectively absent.

### 1.6.2 Interconnected genelets

When the two genelets are present in solution in stoichiometric amount, their RNA outputs bind quickly to form a double-stranded complex, and therefore the feedback loops become a secondary reaction (by design thermodynamically less favorable than the  $R_1 \cdot R_2$  complex formation). As shown in Figure S2 C, the two genelets only moderately self-repress. The total RNA concentration in solution is high, as shown in the denaturing gel in Figure S2 B, lanes 3 and 4.

When the templates  $[T_1^{tot}]$  and  $[T_2^{tot}]$  are in different ratios, the system behavior is shown in Figure S3. We can plot the resulting initial active template ratio (which corresponds to the

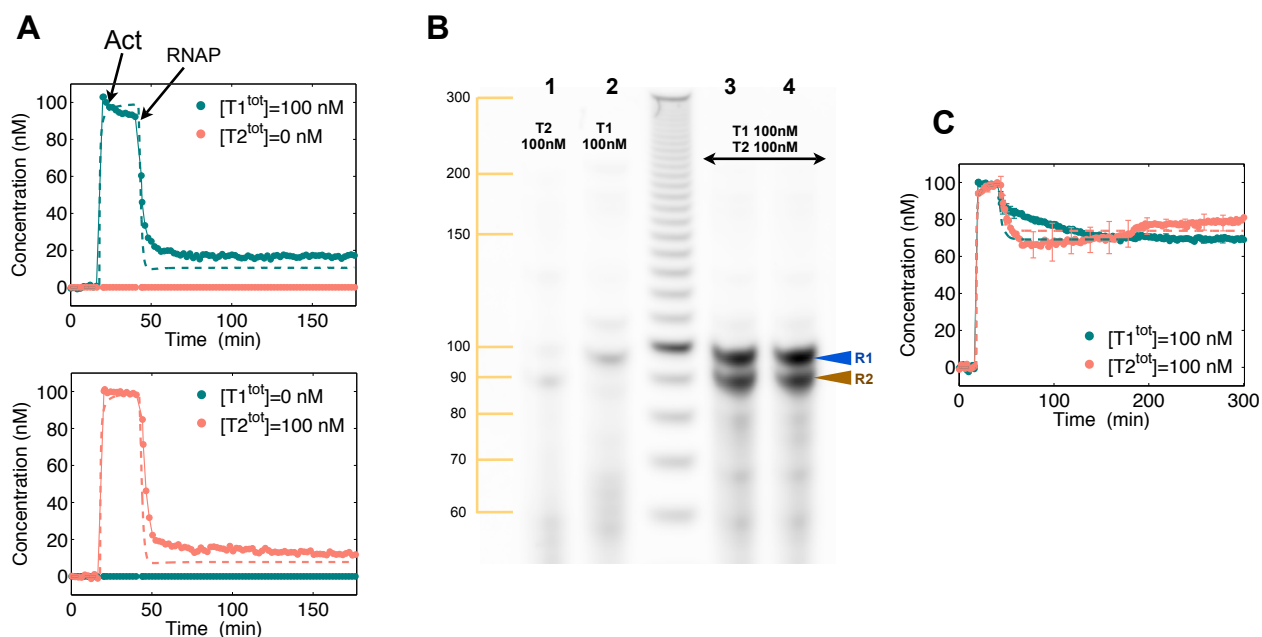


Figure S2: A. Experimental data showing the isolated active genelet concentrations as a function of time: the self-inhibition reaction turns the switches off, and the RNA concentration in solution is negligible, as verified in the gel electrophoresis data in panel B, lanes 1 and 2 (samples taken at steady-state after 2 h). Dashed lines represent numerical trajectories of equations (5), using the fitted parameters in Table S2. B. Denaturing gel image: lanes 1 and 2 show that the switches in isolation self-inhibit and no significant transcription is measured. Lanes 3 and 4 show the total RNA amount in samples from the experiment shown at panel C, taken at steady-state after 2 h. When the genelets are in stoichiometric amount, their flow rates are already balanced and there is only moderate self-inhibition.

total template ratio) versus the steady-state one: we find that the system behaves symmetrically and the steady-state ratio is close to one across all the initial ratios. Therefore, given open loop transcription rates that differ across a factor of 1–3, these results suggest that the system robustly matches the flux of  $R_1$  and  $R_2$ .

### 1.6.3 Flux adaptation

If the concentration of  $[T_i^{tot}]$  and  $[A_i^{tot}]$  is changed over time, the steady-state concentration of active genelets adjusts as shown in Figure S5 A and B. Samples from this set of experiments were analyzed using a denaturing gel: the results are shown in Figure S5 C and D (corresponding to the traces in Figure S5 A and B, respectively) and show the total RNA amount in solution and that  $[R_1^{tot}] \approx [R_2^{tot}]$ , as desired (Figure S5 E and F). The RNA concentrations were estimated using the DNA ladder as a reference. We are aware that this method may result in inaccurate absolute concentration estimates for RNA: however, our objective here is to compare the evolution over time of the relative RNA concentrations. Thus, inaccuracy in the determination of the absolute amount of RNA produced does not affect the measured outcome of our experiments. The adjustment of genelet activity becomes progressively slower over time: the third round of adaptation is consistently slower than the previous two. We attribute this slower adaptation to various phenomena: 1) Decrease of activity of enzymes over time; 2) Accumulation of incomplete degradation products from RNase H hydrolyzation of RNA in RNA-DNA hybrids: these products can be up to 7–8 bases long, and may interfere with the desired inhibition pathways; 3) Abortive transcription of RNA, which could also potentially bind to regulatory domains of DNA activators. Our hypothesis of accumulation of short products over time is validated by the gels shown in Figure S5 C and D (below 60 bases, part of the gel that is not shown, a similar smear is visible).

### 1.6.4 Data fitting

We derived a system of ordinary differential equations (ODEs) starting from mass action kinetics, as described in Section 2.2. The ODE system was numerically fitted using MATLAB (The MathWorks) to fluorescence data in Figures S2 and S3. Only a subset of the parameters was fit using the MATLAB `fmincon` routine. We fit the total RNA polymerase and RNase H concentrations and the rates  $k_{T_i A_i}$ ,  $k_{T_i A_i R_i}$ ,  $k_{A_i R_i}$ ,  $k_{R_1 R_2}$ ,  $k_{R_i T_j}$ , and the parameters  $k_{catON_{ii}}$  and  $k_{catH_{ij}}$ . This specific subset of parameters was chosen because experimental outcomes are chiefly affected by branch migration rates (which are tunable by design of the toehold lengths), enzyme concentration, and enzyme catalytic rates. The concentration and composition of the transcription enzyme mix for the T7 Megashortscript kit are not disclosed by Ambion, but available literature suggests that additional enzymes, such as pyrophosphatase, are present in the mix, Milburn et al. [U. S. Patent 5256555, 1993]. We neglected reactions associated with the possibly unknown amount of pyrophosphatase in the mix. The concentration of RNase H is also not disclosed by Ambion; we did not run separate experiments to fit exclusively the degradation rate parameters. A table reporting all the parameters is in Section 2, Tables S1 and S2.

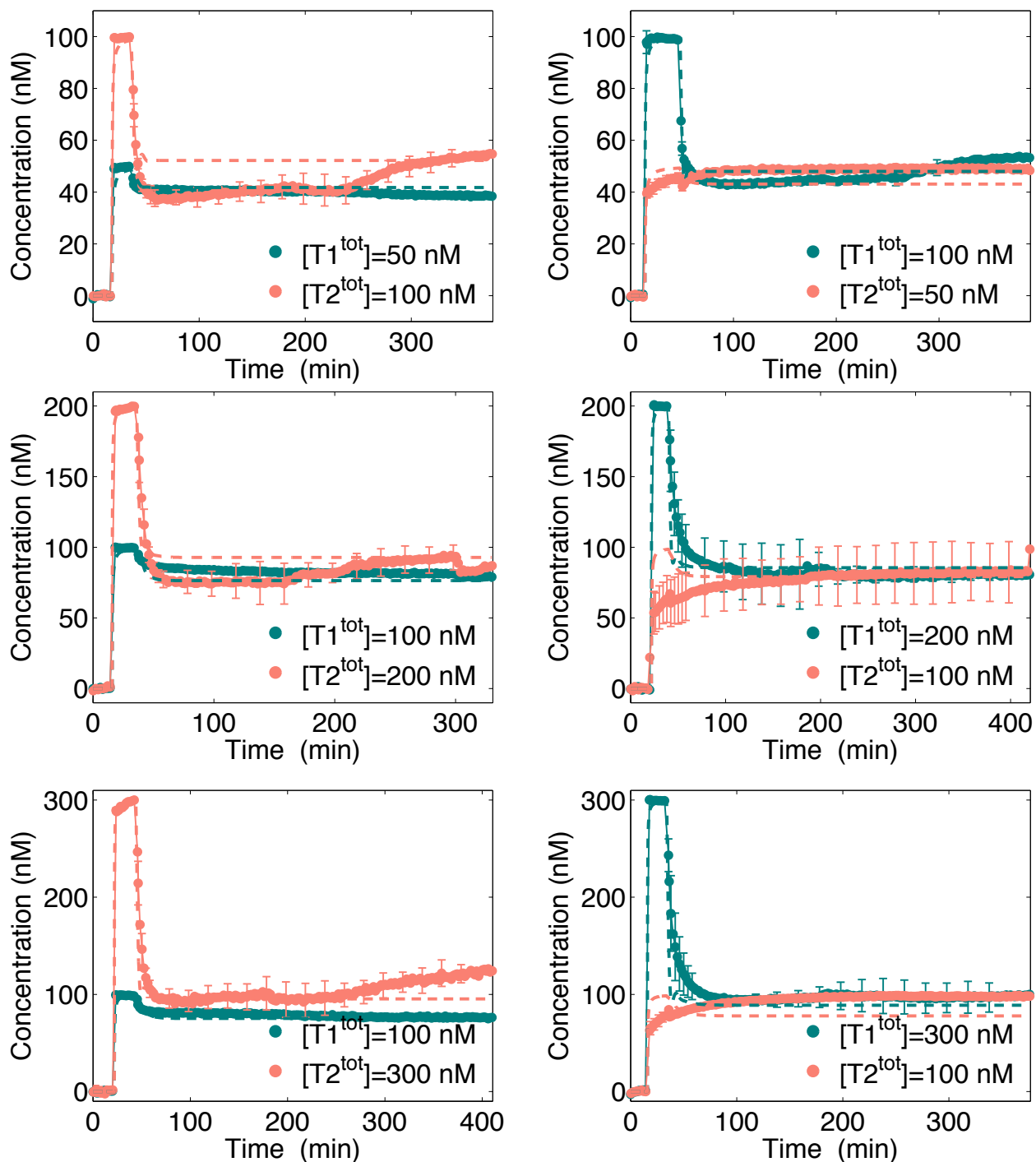


Figure S3: Concentration of active genelets over time at different total templates concentration. The concentration of activators is always stoichiometric to the amount of corresponding template. Dashed lines in all the figures correspond to numerical simulations for model (5), using the parameters in Table S2.

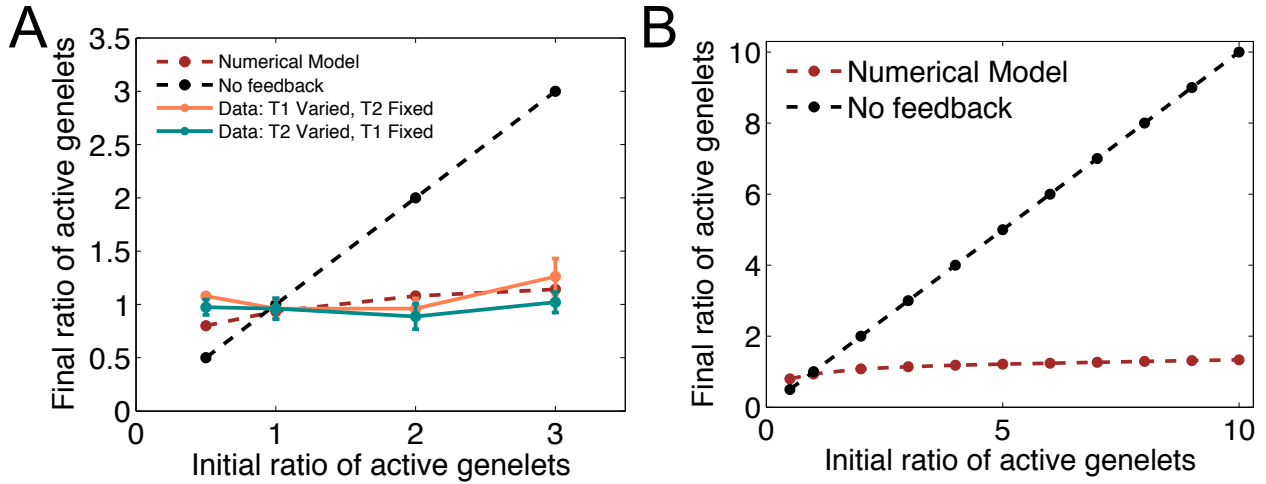
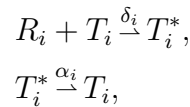


Figure S4: A: Plot summarizing the data shown at Figure S3, overlaid with the predictions of the numerical model (5), using fitted parameters shown in Table S2. B: Predicted initial versus final genelets activity for ratios up to 10:1, according to our model (5) and parameters at Table S2.

## 2 Modeling and numerical analysis: two-gene flux matching system

### 2.1 Simple model system: derivation of nullclines and rate matching conditions

We consider a system composed of two generating species  $T_1$  and  $T_2$ , whose products  $R_1$  and  $R_2$  interact to form a complex  $P = R_1 \cdot R_2$ . We introduce negative autoregulation to minimize the concentration of product that is not used to form the output complex (Figure S6). Free molecules of  $R_i$ ,  $i = 1, 2$ , bind to active  $T_i$ , thereby inactivating it:



where  $T_i^*$  is an inactive complex. We assume that  $T_i^{tot} = T_i + T_i^*$ , and that  $T_i^*$  naturally reverts to its active state with a first-order rate  $\alpha_i$ . The total amount of  $R_i$  is  $[R_i^{tot}] = [R_i] + [T_i^*] + [P]$ . The corresponding differential equations are:

$$\begin{aligned} \frac{d[T_i]}{dt} &= \alpha_i ([T_i^{tot}] - [T_i]) - \delta_i [R_i][T_i], \\ \frac{d[R_i]}{dt} &= \beta_i [T_i] - k [R_i][R_j] - \delta_i [R_i][T_i]. \end{aligned} \quad (1)$$

For illustrative purposes, these differential equations are solved numerically. The parameters chosen are:  $\alpha_1 = \alpha_2 = 3 \cdot 10^{-4}$  /s,  $\beta_1 = \beta_2 = 0.01$  /s,  $\delta_1 = \delta_2 = 5 \cdot 10^2$  /M/s, and  $k = 2 \cdot 10^3$  /M/s. An imbalance in the production rates of  $R_1$  and  $R_2$  is created by setting

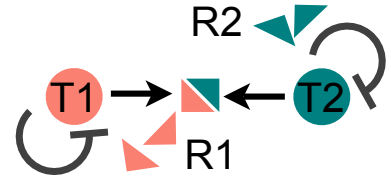


Figure S6: Our two-gene negative feedback architecture

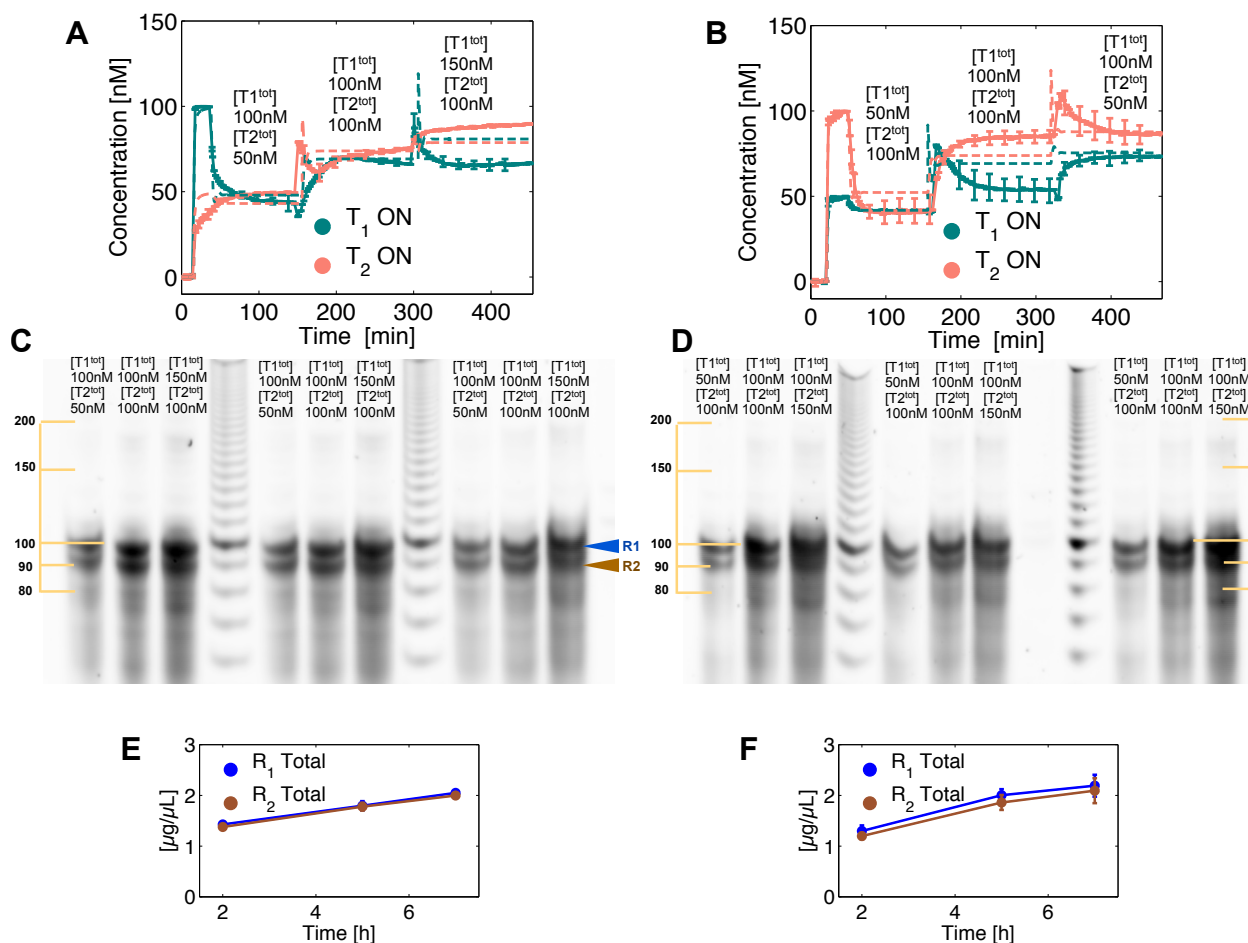


Figure S5: A and B. Fluorescent traces showing the adaptation of the active fraction of genelets, when the total amount of templates is varied over time. C and D. Samples from the experiments shown in panels A and B, respectively, were analyzed with gel electrophoresis. E and F show the concentrations of RNA species, estimated from the gel samples.

$[T_1](0) = [T_1^{tot}] = 100$  nM and  $[T_2](0) = [T_2^{tot}] = 200$  nM, while  $[R_1](0) = [R_2](0) = 0$ . The overall result of this feedback interconnection is that the mismatch in the flow rate of  $R_1$  and  $R_2$  is reduced, as shown in Figure S7. The flow rate is defined as the derivative of  $[R_i^{tot}]$ . The flow rate mismatch is defined as the absolute value of the difference between the two flows. The effect of changing the feedback strength, for simplicity chosen as  $\delta_1 = \delta_2$ , is shown in Figure S8: the figure shows the mean active fraction of  $[T_i]$  and the mean flow mismatch, averaged over the last two hours of a trajectory simulated for 10 hours.

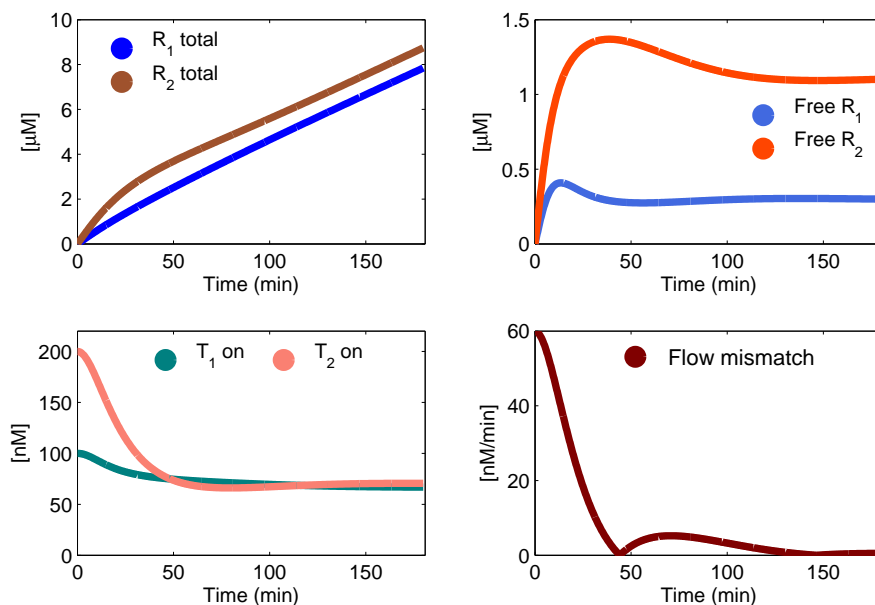


Figure S7: Numerical simulation showing the solution to the two-gene negative feedback architecture for flux matching modeled with equations (1). The flow mismatch between  $R_1$  and  $R_2$  is shown in the bottom-right panel.

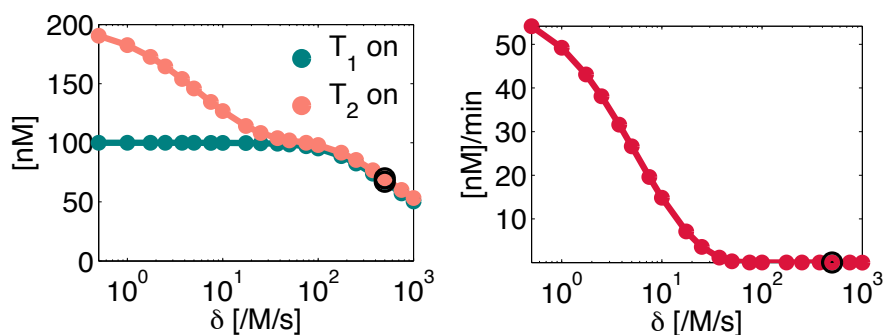


Figure S8: Numerical simulation showing genelet activity and mismatch over a range of values for the negative feedback parameter  $\delta$ .

It is possible to examine the nullclines relating  $T_1$  and  $T_2$ , and find the equilibria  $\bar{T}_1$  and  $\bar{T}_2$

as intersection of these nullclines:

$$\begin{aligned}\dot{T}_i = 0 &\implies R_i = \frac{\alpha_i(T_i^{tot} - T_i)}{\delta_i T_i}, \\ \dot{R}_i = 0 &\implies R_i = \frac{\beta_i T_i}{k R_j + \delta_i T_i}.\end{aligned}$$

To simplify the derivation, we set  $\delta_1 = \delta_2 = \delta$ ,  $\beta_1 = \beta_2 = \beta$ ,  $\alpha_1 = \alpha_2 = \alpha$ . Equating the two expressions for  $R_i$ , we get the following equations (for  $i = 1, 2$  and  $j = 1, 2$ ):

$$\left(\frac{\alpha}{\delta}\right)^2 k \left(\frac{T_i^{tot} - T_i}{T_i}\right) \left(\frac{T_j^{tot} - T_j}{T_j}\right) + \alpha(T_i^{tot} - T_i) - \beta T_i = 0.$$

We can find an expression of the nullclines by introducing a change of variables  $u = \left(\frac{T_1^{tot} - T_1}{T_1}\right)$  and  $v = \left(\frac{T_2^{tot} - T_2}{T_2}\right)$ , and defining  $\phi_1 = \psi_1 = \left(\frac{\alpha}{\delta}\right)^2 k$ ,  $\phi_2 = \alpha T_1^{tot}$ ,  $\psi_2 = \alpha T_2^{tot}$ ,  $\phi_3 = \beta T_2^{tot}$ , and finally  $\psi_3 = \beta T_1^{tot}$ :

$$u^2(\phi_1 v) + u(\phi_1 v + \phi_2 - \phi_3 \frac{1}{1+v}) - \phi_3 \frac{1}{1+v} = 0, \quad (2)$$

$$v^2(\psi_1 u) + v(\phi_1 u + \psi_2 - \psi_3 \frac{1}{1+u}) - \psi_3 \frac{1}{1+u} = 0. \quad (3)$$

The roots of the equations above represent the nullclines of the system. Because all the parameters in these equations are positive, there is always a single root. The nullclines are numerically solved, for varying  $\delta$ , in Figure S9.

A condition for flow matching at steady-state can be derived as follows:

$$\begin{aligned}\dot{R}_1 - \dot{R}_2 &= 0, \\ \beta_1 T_1 - \delta_1 T_1 R_1 &= \beta_2 T_2 - \delta_2 T_2 R_2.\end{aligned}$$

Substituting the expressions for  $R_1$  and  $R_2$  that can be derived by setting  $\dot{T}_1 = 0 = \dot{T}_2$ , we get:

$$\beta_1 \bar{T}_1 - \alpha_1 (T_1^{tot} - \bar{T}_1) = \beta_2 \bar{T}_2 - \alpha_2 (T_2^{tot} - \bar{T}_2).$$

Taking  $\alpha_1 = \alpha_2 = \alpha$ ,  $\beta_1 = \beta_2 = \beta$  we get:

$$\bar{T}_2 = \bar{T}_1 + \frac{\alpha}{\alpha + \beta} (T_2^{tot} - T_1^{tot}). \quad (4)$$

The flow matching condition above is shown in Figure S9, orange line (also shown in the main paper). If  $\beta \gg \alpha$ , i.e., the production of  $R_i$  is much faster than the generating species  $T_i$  inactivation rate, then the condition can be rewritten as:

$$\bar{T}_1 \approx \bar{T}_2.$$

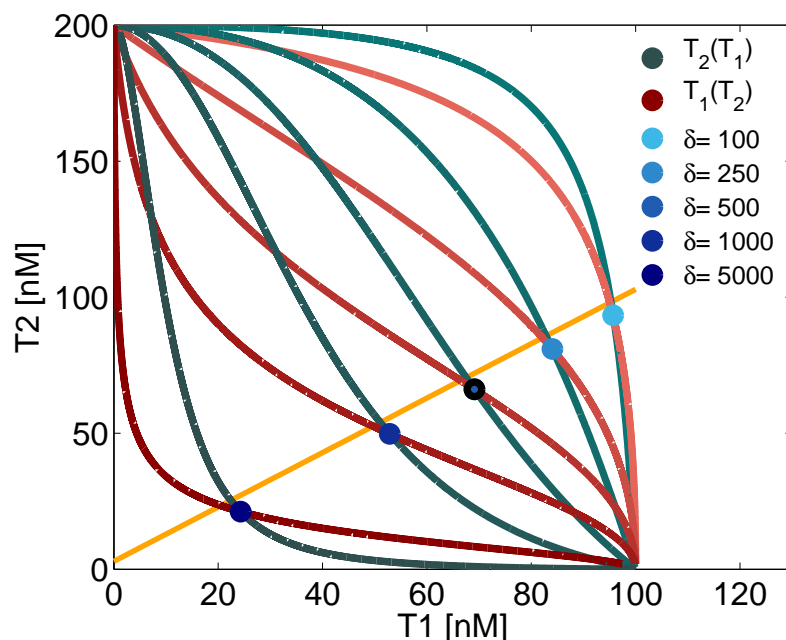


Figure S9: Nullclines computed for different values of negative feedback rate  $\delta$ , and flux matching condition (orange)

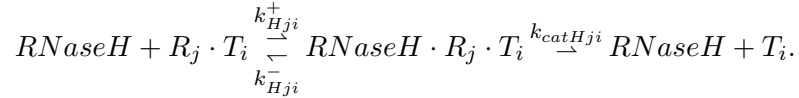
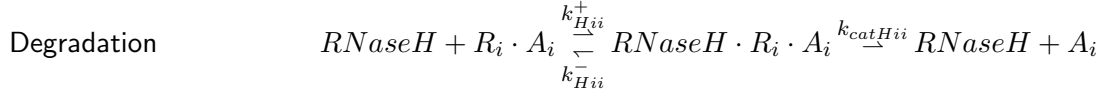
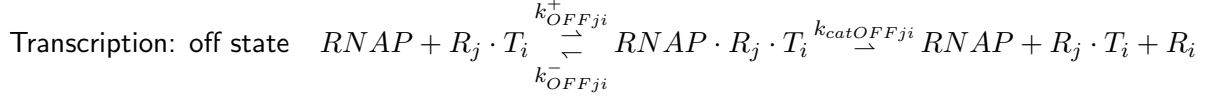
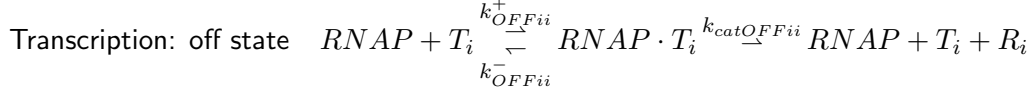
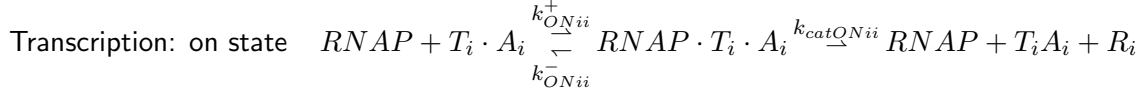
## 2.2 Differential equations modeling the experimental implementation

Based on our design specifications and the resulting molecular interactions, we built a model for the system starting from the list of occurring chemical reactions. The switches  $T_i$  and  $T_j$  can have three possible states: the on state where activator and template are bound and form the complex  $T_i A_i$ ; the off state given by free  $T_i$ ; the off state represented by  $R_j$  bound to  $T_i$  forming  $T_i R_j$ . An off state still allows for *RNAP* weak binding and transcription. Throughout this derivation, the dissociation constants are omitted when assumed to be negligible. It is hypothesized that the concentration of enzymes is considerably lower than that of the DNA molecules, allowing the classical steady-state assumption for Michaelis-Menten kinetics.

Branch migration and hybridization reactions among nucleic acids are, for  $i \in \{1, 2\}$ ,  $j \in \{2, 1\}$ :

Activation	$T_i + A_i \xrightarrow{k_{T_i A_i}} T_i \cdot A_i$
Inhibition	$R_i + T_i \cdot A_i \xrightarrow{k_{T_i A_i R_i}} R_i \cdot A_i + T_i$
Annihilation	$R_i + A_i \xrightarrow{k_{A_i R_i}} R_i \cdot A_i$
Output formation	$R_i + R_j \xrightarrow{k_{R_i R_j}} R_i \cdot R_j$
Undesired hybridization	$R_j + T_i \xrightarrow{k_{R_j T_i}} R_j \cdot T_i$

The enzymatic reactions are, for  $i \in \{1, 2\}$ ,  $j \in \{2, 1\}$ :



Using the law of mass action, we derive the following ODEs:

$$\begin{aligned} \frac{d}{dt}[T_i] &= -k_{T_i A_i}[T_i][A_i] + k_{T_i A_i R_i}[R_i][T_i \cdot A_i] - k_{R_j T_i}[R_j][T_i] + k_{catHji}[RNaseH \cdot R_j \cdot T_i], \\ \frac{d}{dt}[A_i] &= -k_{T_i A_i}[T_i][A_i] - k_{A_i R_i}[R_i][A_i] + k_{catHii}[RNaseH \cdot R_i \cdot A_i], \\ \frac{d}{dt}[R_i] &= -k_{R_i R_j}[R_i][R_j] - k_{T_i A_i R_i}[R_i][T_i \cdot A_i] - k_{R_i T_j}[R_i][T_j] - k_{A_i R_i}[R_i][A_i] \\ &\quad + k_{catONii}[RNAP \cdot T_i \cdot A_i] + k_{catOFFii}[RNAP \cdot T_i] + k_{catOFFji}[RNAP \cdot R_j \cdot T_i], \\ \frac{d}{dt}[R_i \cdot R_j] &= +k_{R_i R_j}[R_i][R_j], \\ \frac{d}{dt}[R_j \cdot T_i] &= +k_{R_j T_i}[R_j][T_i] - k_{catHji}[RNaseH \cdot R_j \cdot T_i]. \end{aligned} \tag{5}$$

The molecular complexes appearing at the right-hand side of these equations can be expressed using mass conservation:

$$[T_i \cdot A_i] = [T_i^{tot}] - [T_i] - [R_j \cdot T_i], \quad [R_i \cdot A_i] = [A_i^{tot}] - [A_i] - [T_i \cdot A_i].$$

We assume that binding of enzymes to their substrate is faster than the subsequent catalytic step, and that the substrate concentration is larger than the total amount of enzyme. These assumptions allow us to use the standard Michaelis-Menten quasi-steady-state expressions. The Michaelis-Menten coefficients can be immediately defined; for instance, for the ON state of the template, define:  $k_{MONii} = \frac{k_{ONii}^- + k_{catONii}}{k_{ONii}^+}$ . Then we find:

$$\begin{aligned} [RNAP^{tot}] &= [RNAP] \left( 1 + \frac{[T_1 \cdot A_1]}{k_{MON11}} + \frac{[T_1]}{k_{MOFF11}} + \frac{[T_2 \cdot A_2]}{k_{MON22}} + \frac{[T_2]}{k_{MOFF22}} + \frac{[R_2 \cdot T_1]}{k_{MOFF21}} + \frac{[R_1 \cdot T_2]}{k_{MOFF12}} \right), \\ [RNaseH^{tot}] &= [RNaseH] \left( 1 + \frac{[R_1 \cdot A_1]}{k_{MH11}} + \frac{[R_2 \cdot A_2]}{k_{MH22}} + \frac{[R_2 \cdot T_1]}{k_{MH21}} + \frac{[R_1 \cdot T_2]}{k_{MH12}} \right). \end{aligned}$$

We can easily rewrite these equations as  $[RNAP] = \frac{[RNAP^{tot}]}{P}$  and  $[RNaseH] = \frac{[RNaseH^{tot}]}{H}$ , with a straightforward definition of the coefficients  $P$  and  $H$ . Finally:

$$\begin{aligned} [RNAP \cdot T_i \cdot A_i] &= \frac{[RNAP^{tot}] [T_i \cdot A_i]}{P \cdot k_{MONii}}, \\ [RNAP \cdot R_j \cdot T_i] &= \frac{[RNAP^{tot}] [R_j \cdot T_i]}{P \cdot k_{MOFFji}}, \\ [RNAP \cdot T_i] &= \frac{[RNAP^{tot}] [T_i]}{P \cdot k_{MOFFii}}, \\ [RNaseH \cdot R_i \cdot A_i] &= \frac{[RNaseH^{tot}] [R_i \cdot A_i]}{H \cdot k_{MHii}}, \\ [RNaseH \cdot R_j \cdot T_i] &= \frac{[RNaseH^{tot}] [R_j \cdot T_i]}{H \cdot k_{MHji}}, \end{aligned}$$

which can be substituted in equations (5). We note that our numerical fits result in an estimated  $RNAP$  concentration of about 100 nM: thus, in a subset of our experiments the substrate and enzyme concentrations are actually comparable, breaking down one of the assumptions required for a quasi-steady-state approximation. Nevertheless, our model overall captures the system dynamics satisfactorily.

The nonlinear set of equations (5) was solved numerically using MATLAB ode23 routine.

**Preliminary numerical analysis** Prior to designing DNA strands and testing the system with wet lab experiments, we ran numerical simulations using equations (5) using parameters reported in Table S1. These parameters are consistent with those in Kim et al. [2006], which were fitted from data obtained on a transcriptional system with identical promoter/branch migration design specifications and sequence content; thus, we refer the reader to Kim et al. [2006] for an accurate discussion and comparison to other branch migration, transcription, and degradation parameters found in the literature. Figure S10 shows the system trajectories that correspond to zero initial conditions for  $[A_i]$  and  $[R_i]$ , while the complexes  $[T_1 A_1] = [T_1^{tot}] = 100$  nM,  $[T_2 A_2] = [T_2^{tot}] = 50$  nM,  $[A_1^{tot}] = 100$  nM and  $[A_2^{tot}] = 50$  nM. (The simulation first allows for equilibration of all the DNA strands in the absence of enzymes. Only the portion of trajectories after addition of enzymes is shown.) The total concentration of enzymes was assumed to be  $[RNAP^{tot}] = 80$  nM and  $[RNaseH^{tot}] = 8.8$  nM, consistent with typical volumes used in our experiments and with enzyme stock concentrations of about 1–1.25  $\mu$  M Kim and Winfree [2011], Franco et al. [2011]. An example of our numerical simulation results is shown in Figure S10. The behavior of the system proved to be consistent with the traces obtained for the simple model system shown at Figure S7.

**Data fitting results** As already indicated in Section 1.6.4, equations (5) were fitted to all fluorescence data in Figures S2 and S3 simultaneously, using MATLAB routine `fmincon`. Only a subset of the parameters was fit: the total RNA polymerase and RNase H concentrations, and the rates  $k_{T_i A_i}$ ,  $k_{T_i A_i R_i}$ ,  $k_{A_i R_i}$ ,  $k_{R_1 R_2}$ ,  $k_{R_i T_j}$ , and the parameters  $k_{catON_{ii}}$  and  $k_{catH_{ij}}$ . Table S2 lists the results of the data fit; Table S3 reports the constraints used in the fitting procedure. Our fits indicate that the hybridization and branch migration rates fitting these experiments are higher than what found in Kim et al. [2006], Franco et al. [2011]. In particular, the binding rate of the RNA species is higher than expected; hybridization rates for complementary RNA strands of

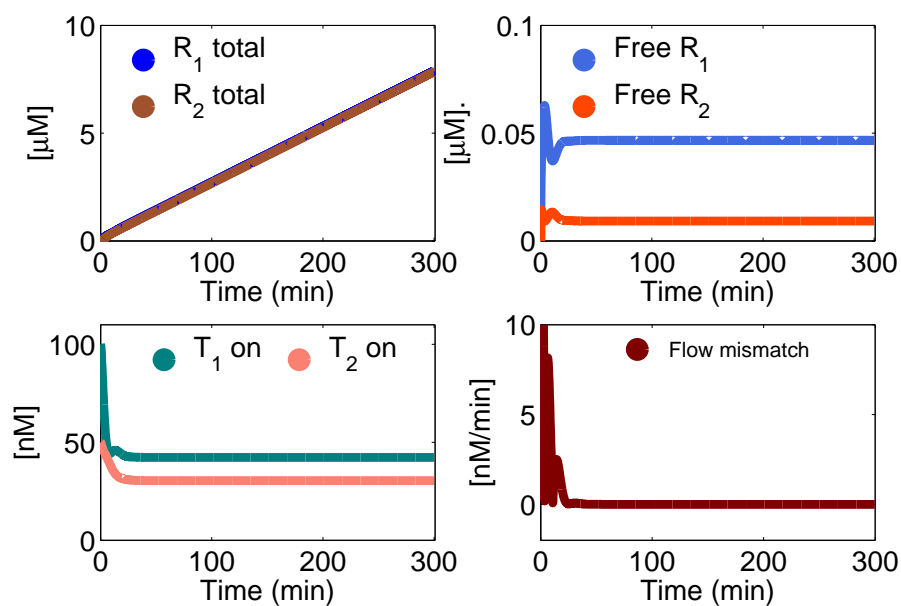


Figure S10: Numerical simulation for equations (5). Parameters are chosen as in Table S1.  $[T_1^{tot}] = [A_1^{tot}] = 100$  nM,  $[T_2^{tot}] = [A_2^{tot}] = 50$  nM,  $[RNAP^{tot}] = 80$  nM, and  $[RNaseH^{tot}] = 8.8$  nM. These results are consistent with those of the simple model proposed in equations (1), and analyzed numerically in Figure S7.

Table S1: Preliminary Simulation Parameters for Equations (5)

Units: $[1/M/s]$	Units: $[1/s]$	Units: $[M]$
$k_{T_i A_i} = 4 \cdot 10^4$	$k_{catON_{ii}} = 0.06$	$k_{MON_{ii}} = 250 \cdot 10^{-9}$
$k_{T_i A_i R_i} = 5 \cdot 10^4$	$k_{catOFF_{ii}} = 1 \cdot 10^{-3}$	$k_{MOFF_{ii}} = 1 \cdot 10^{-6}$
$k_{A_i R_i} = 5 \cdot 10^4$	$k_{catOFF_{ij}} = .5 \cdot 10^{-3}$	$k_{MOFF_{ij}} = 1 \cdot 10^{-6}$
$k_{R_i T_j} = 1 \cdot 10^4$	$k_{catH_{ii}} = .1$	$k_{MH_{ii}} = 50 \cdot 10^{-9}$
$k_{R_i R_j} = 1 \cdot 10^6$	$k_{catH_{ji}} = .1$	$k_{MH_{ji}} = 50 \cdot 10^{-9}$
Units: $[M]$	Units: $[M]$	
$[RNAP^{tot}] = 80 \text{ nM}$	$[RNaseH^{tot}] = 8.8 \text{ nM}$	

similar length have (to our knowledge) not been assessed before. The expected concentrations of RNA polymerase and RNase H and their  $k_{cat}$  values are also higher than in previous studies Kim et al. [2006], Franco et al. [2011], where lower hybridization rates were attributed to the presence of incomplete degradation products from RNase H hydrolyzation of DNA/RNA hybrids. These short products, known to have length up to 7–8 bases, may interfere with desired regulatory pathways Kim and Winfree [2011]. Because the activity and efficiency of off-the-shelf enzymes is known to considerably vary from batch to batch Kim and Winfree [2011], it is reasonable to hypothesize that the RNA polymerase and RNase H batches used in this set of experiments had particularly high activity and low occurrence of incomplete transcription/degradation which can slow down other reactions. Indeed, the accumulation of these incomplete products over time may be the reason for slower dynamics observed in our adaptation experiments in Figure S5.

Table S2: Fitted Parameters for (5); other parameters were left unvaried with respect to Table S1

Units: $[1/M/s]$	Units: $[1/s]$
$k_{T_i A_i} = 6.6 \cdot 10^5$	$k_{catON_{11}} = 0.1, k_{catON_{22}} = 0.09$
$k_{T_1 A_1 R_1} = 0.7 \cdot 10^5, k_{T_2 A_2 R_2} = 0.6 \cdot 10^5$	$k_{catH_{ii}} = .09$
$k_{A_1 R_1} = k_{A_2 R_2} = 4.4 \cdot 10^5$	$k_{catH_{21}} = .03, k_{catH_{12}} = .02$
$k_{R_i R_j} = 4.9 \cdot 10^6$	
Units: $[M]$	Units: $[M]$
$[RNAP^{tot}] = 100 \text{ nM}$	$[RNaseH^{tot}] = 20 \text{ nM}$

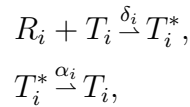
Table S3: Fitting constraints for parameters in Table S2.

Parameter	Lower Bound	Upper Bound
$k_{T_i A_i}$	$10^3$	$5 \cdot 10^5$
$k_{T_i A_i R_i}$	$10^3$	$5 \cdot 10^5$
$k_{A_i R_i}$	$10^3$	$5 \cdot 10^5$
$k_{R_i R_j}$	$10^3$	$5 \cdot 10^5$
$k_{catON_{ii}}$	0.01	0.1
$k_{catH_{ii}}$	0.001	0.1
$[RNAP^{tot}]$	$15 \cdot 10^{-9}$	$100 \cdot 10^{-9}$
$[RNaseH^{tot}]$	$5 \cdot 10^{-9}$	$20 \cdot 10^{-9}$

### 3 Modeling and numerical analysis: Scalability of the negative feedback scheme for flux regulation

#### 3.1 Simple model system

We consider now  $n$  generating species  $T_i$ , outputting interacting products  $R_i$ , and we explore different feedback interconnection topologies. Initial studies on scalability were outlined in Giordano et al. [2013]. ODEs were derived using mass action kinetics and used for numerical simulation of three- and four-component networks. Negative autoregulation is implemented, as for smaller networks, with a self-repression scheme: when an output is in excess relative to the effectively used amount, it down-regulates its own production rate.



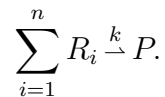
where  $T_i^*$  is an inactive complex. We assume that  $[T_i^{tot}] = [T_i] + [T_i^*]$  and that  $T_i^*$  spontaneously reverts to its active state with a first-order rate  $\alpha_i$ . The corresponding differential equation describing the template dynamics is the same regardless of the topology:

$$\frac{d[T_i]}{dt} = \alpha_i ([T_i^{tot}] - [T_i]) - \delta_i [R_i][T_i], \quad i = 1, \dots, n.$$

Depending on the chosen interaction/binding topology for the products  $R_i$ , we find that the system exhibits different behaviors, as shown in the following sections.

##### 3.1.1 Single product topology

A single product topology occurs when a single complex  $P$  is formed by the simultaneous interaction of all the  $n$  outputs:



The corresponding differential equations are

$$\begin{aligned} \frac{d[R_i]}{dt} &= \beta_i [T_i] - \delta_i [R_i][T_i] - k \prod_{i=1}^n [R_i], \\ \frac{d[P]}{dt} &= k \prod_{i=1}^n [R_i] \end{aligned}$$

and the total amount of  $R_i$  is  $[R_i^{tot}] = [R_i] + [T_i^*] + [P]$ . Figure S11 shows the numerical solutions to the ODEs for  $n = 3$  and  $n = 4$ . Even though the initial total amounts of  $T_i$  are different, the concentration of active  $T_i$  (bottom left panel) gradually decreases and the flow mismatches (namely the differences in absolute value between any two production rates, shown in the bottom right panel) are considerably reduced with a fast time response. We can notice that the response is slower in the case of 4 interconnected species. The quantity of produced  $R_i$  (upper left panel) is of course increasing. With respect to the other topologies, as we will see, the single product topology leads to a much higher amount of free  $R_i$  (upper right panel), which can be considered waste because it is not used in the product formation.

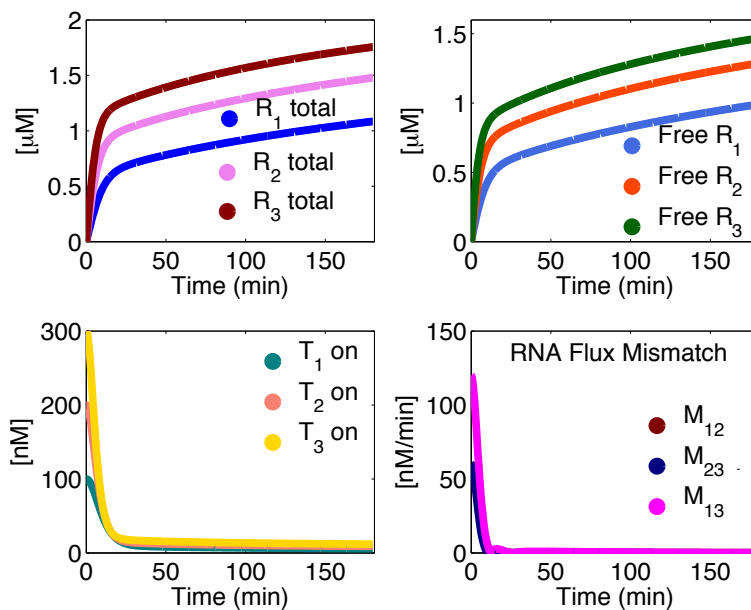
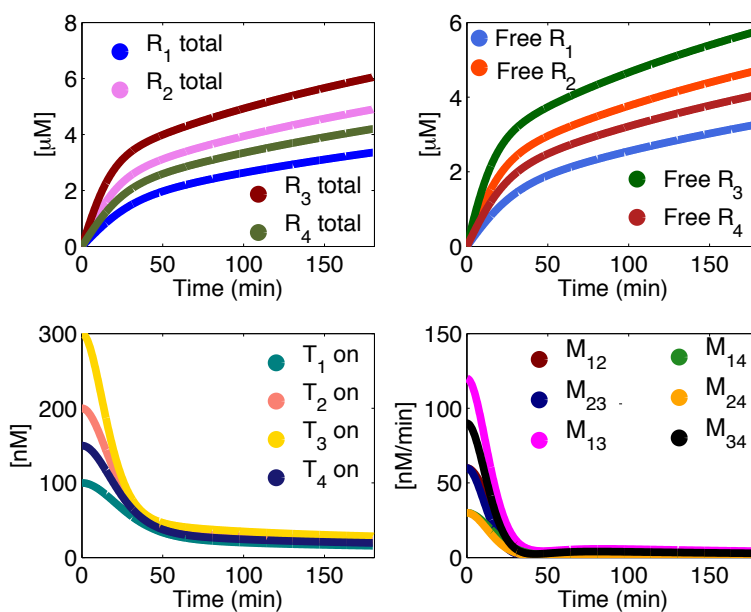
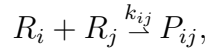
(a) single product,  $n = 3$ (b) single product,  $n = 4$ 

Figure S11: Example traces from numerical simulations: single product topology, negative feedback scheme.

### 3.1.2 Handshake and neighbor topologies

A network of  $n$  generating species  $T_i$  may be designed to produce different subcomponents, that may later assemble into a larger product. In this scenario, we can take two extreme cases: the neighbor topology, when each output participates in at most two subcomponents, and the handshake topology, when each output participates in  $n - 1$  subcomponents. We thus have the generation of pairwise products  $P_{ij}$ ; in the handshake case  $i, j = 1, \dots, n, j \neq i$ , while in the neighbor case  $i = 1, \dots, n, j = i - 1, i + 1$  and when  $i = 1, i - 1 = n$ , when  $i = n, i + 1 = 1$ , to close the loop. It is worth noticing that, in the case  $n = 3$ , the two topologies coincide. The reactions corresponding to product generation are



which lead to the following ODEs:

$$\begin{aligned} \frac{d[R_i]}{dt} &= \beta_i [T_i] - \delta_i [R_i][T_i] - \sum_j k_{ij} [R_i][R_j], \\ \frac{d[P_{ij}]}{dt} &= k_{ij} [R_i][R_j]. \end{aligned}$$

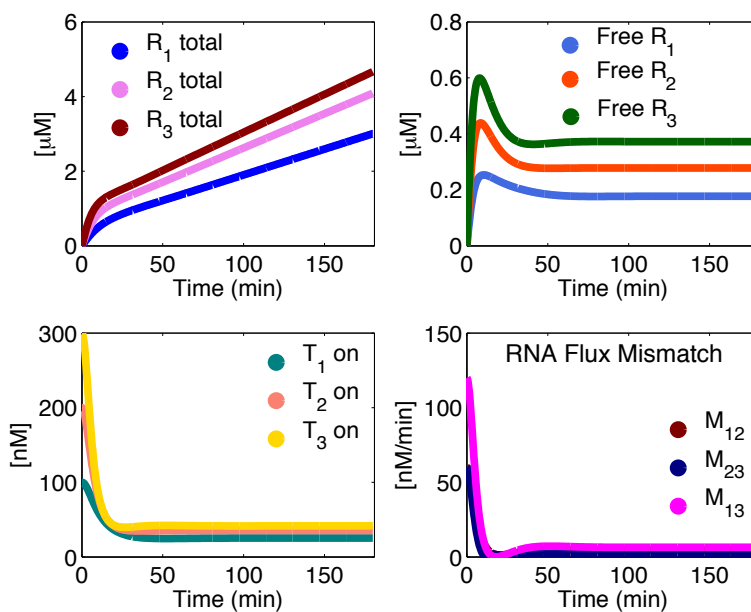
The total amount of  $R_i$  is  $[R_i^{tot}] = [R_i] + [T_i^*] + \sum_j [P_{ij}]$ . Figure S12 shows the numerical solutions to the ODEs for  $n = 3$ , and for  $n = 4$  in the handshake connection case. As for the single product topology, even though we initially have different total amounts of active  $T_i$ , the concentration of active  $T_i$  decreases and the flux mismatches are considerably reduced with a fast time response. Although the quantity of produced  $R_i$  is increasing, the feedback control reduces and keeps bounded the amount of free  $R_i$ , which can be considered waste.

### 3.1.3 Parameters

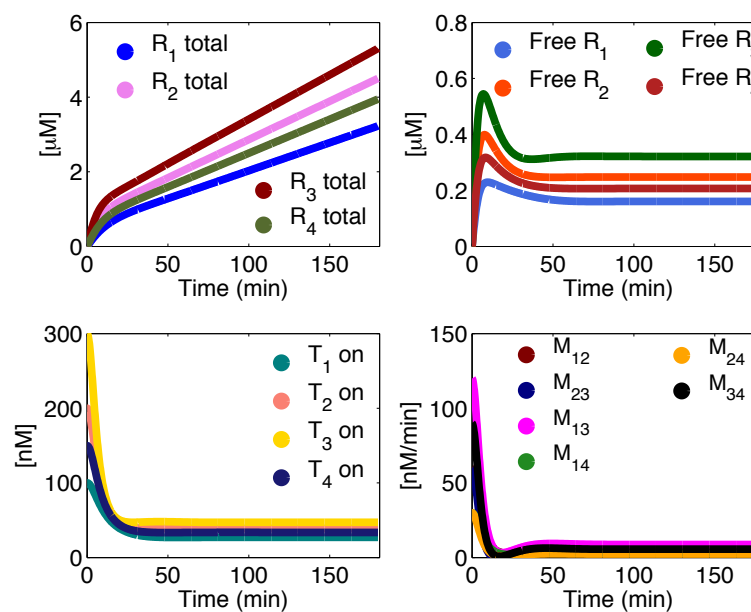
The parameters chosen in our simulations are:  $k_{ij} = 2 \cdot 10^3$  /M/s for the handshake/neighbor topology and  $k = 6 \cdot 10^3$  /M/s for the single product topology,  $\delta_i = 5 \cdot 10^3$  /M/s,  $\alpha_i = 3 \cdot 10^{-4}$  /s,  $\beta_i = 1 \cdot 10^{-2}$  /s,  $[T_1^{tot}] = 100$  nM,  $[T_2^{tot}] = 200$  nM,  $[T_3^{tot}] = 300$  nM,  $[T_4^{tot}] = 150$  nM. An imbalance in the production rates of  $R_i$  is created by setting  $[T_i](0) = [T_i^{tot}]$ , while  $[R_i](0) = 0$ .

### 3.1.4 Performance overview of the different topologies as a function of key parameters

We numerically explored the behavior of the different network topologies for  $n = 4$  as a function of the feedback parameter  $\delta$  and of the rate of activation  $\alpha$ . Figures S13, S14 and S15 show the network response in terms of active percentage of  $T_i$  ( $[T_i]/[T_i^{tot}] \cdot 100$ ), flow mismatch (computed as in the previous cases) and response time (defined as the time it takes for the active  $T_i$  trajectory to go from  $[T_i(0)] - 10\% \Delta$  to  $[T_i(0)] - 90\% \Delta$ , where  $\Delta$  is the difference between its initial value  $[T_i(0)]$  and its steady state value). We solved the differential equations for a time span of 10 hours and averaged the trajectories for active  $T_i$  and for the computed mismatch over the last simulation hour.  $\delta$  varies logarithmically from a tenth to a thousand times its nominal value;  $\alpha$  varies from a hundredth to five times its nominal value. In each figure, pink squares mark the nominal behavior of the system (all parameters are identical to those listed in Section 3.1.3).



(a) handshake/neighbor,  $n = 3$



(b) handshake,  $n = 4$

Figure S12: Example traces from numerical simulations: handshake/neighbor topologies, negative feedback scheme.

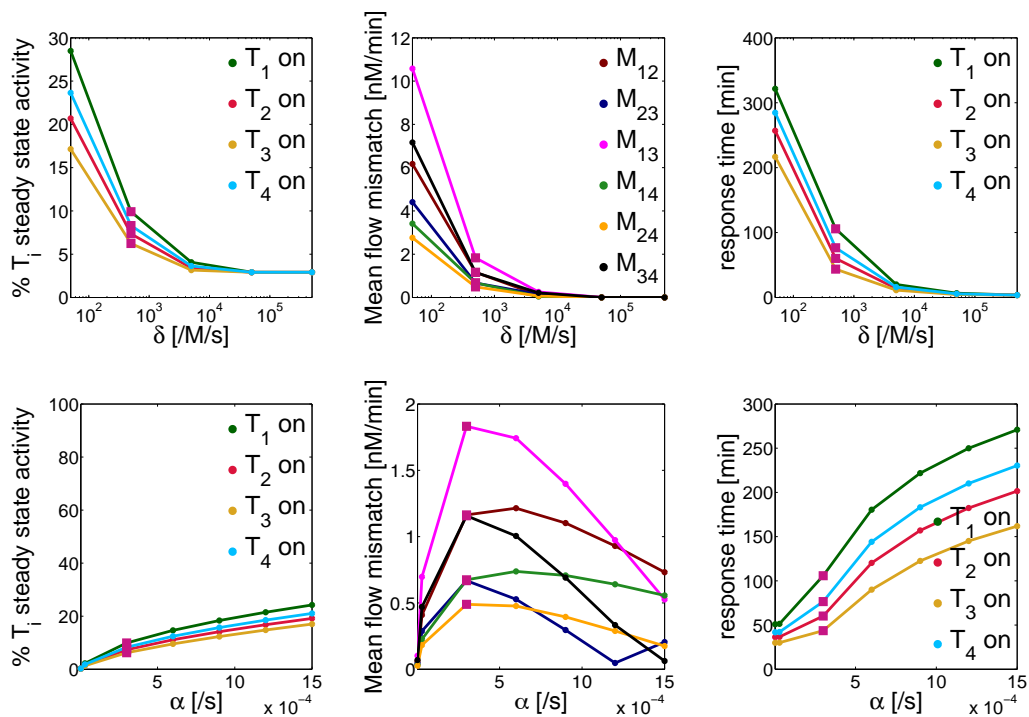


Figure S13: Simulations for the negative feedback, single product topology: parameter sensitivity analysis.

In all network topologies, a large negative feedback parameter  $\delta$  yields a lower mismatch and decreases the response time; however, large  $\delta$  clearly reduces the steady state activity of  $T_i$ . In the handshake and neighbor topologies, a larger value of the spontaneous reactivation parameter  $\alpha$  yields higher  $T_i$  steady state activity, a larger mismatch, and a shorter response time. On the contrary, in the single product topology larger  $\alpha$ , despite yielding higher  $T_i$  steady state activity, dramatically increases the response time, while the mismatch does not monotonically increase.

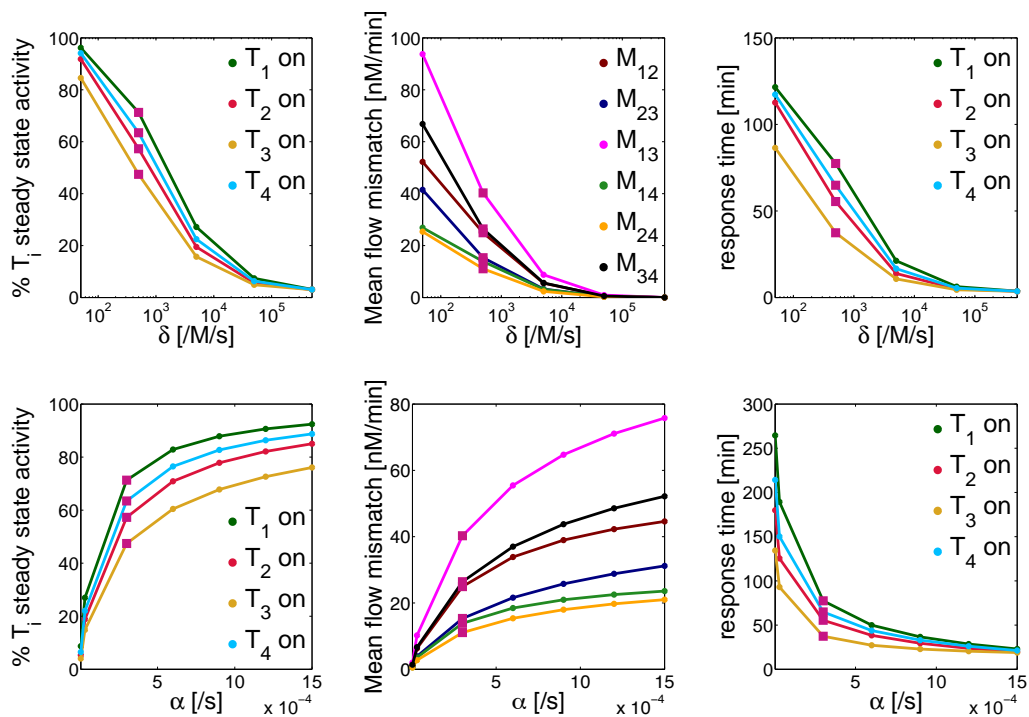


Figure S14: Simulations for the negative feedback, handshake topology: parameter sensitivity analysis.

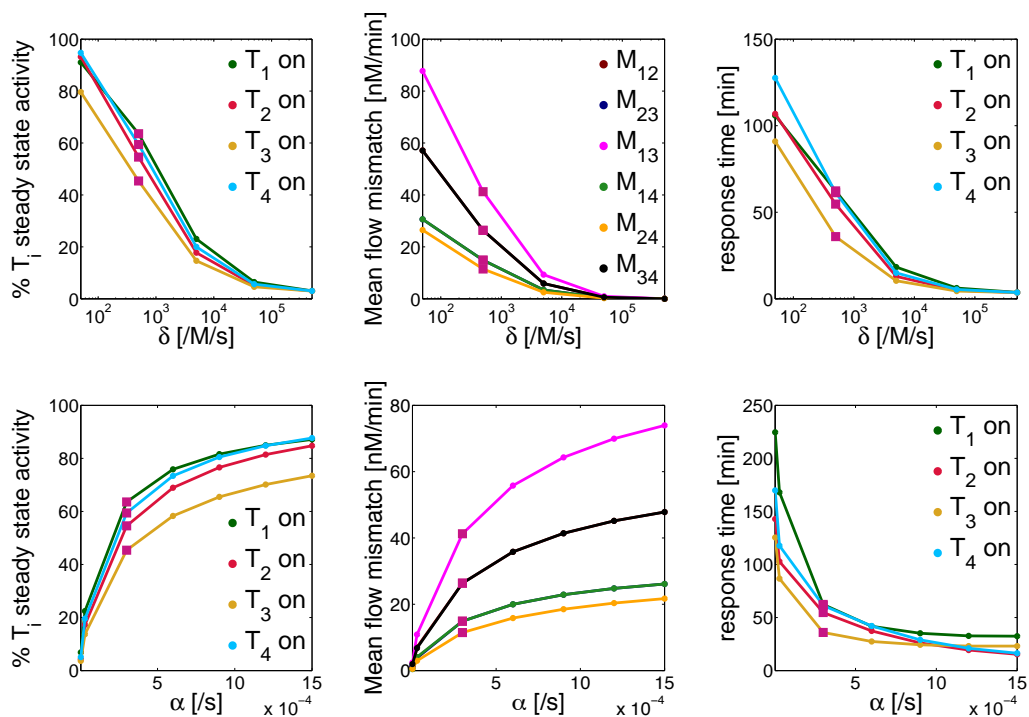


Figure S15: Simulations for the negative feedback, neighbor topology: parameter sensitivity analysis.

## 4 Positive feedback architecture for a two-gene system. Modeling and a viable experimental implementation

### 4.1 Simple model system: derivation of nullclines and rate matching conditions

As done for the negative feedback architecture, we consider a system composed of two generating species  $T_1$  and  $T_2$ , whose products  $R_1$  and  $R_2$  interact to form a complex  $P = R_1 \cdot R_2$ . We devise a positive feedback interconnection where product in excess upregulates the product in shortage (Figure S16). Free (and thus, in excess) molecules of  $R_i$  bind to inactive  $T_j$  and activate it:

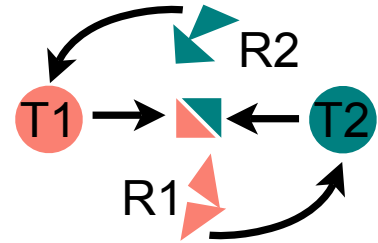
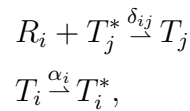


Figure S16: Our two-gene positive feedback architecture

where again  $T_i^*$  is an inactive complex and  $[T_i^{tot}] = [T_i] + [T_i^*]$ . The total amount of  $R_i$  is  $[R_i^{tot}] = [R_i] + [T_j] + [P]$ . We now assume that  $T_i$  naturally reverts to its inactive state with rate  $\alpha_i$ . The corresponding differential equations are

$$\begin{aligned} \frac{d[T_i]}{dt} &= -\alpha_i [T_i] + \delta_{ji} [R_j] ([T_i^{tot}] - [T_i]), \\ \frac{d[R_i]}{dt} &= \beta_i [T_i] - k [R_i] [R_j] - \delta_{ij} [R_i] ([T_j^{tot}] - [T_j]). \end{aligned} \quad (6)$$

This system was initially considered in Franco [2012]. The above differential equations were solved numerically. The parameters were chosen for illustrative purposes as  $\alpha_1 = \alpha_2 = 3 \cdot 10^{-4}$  /s,  $\beta_1 = \beta_2 = 0.01$  /s,  $\delta_1 = \delta_2 = 5 \cdot 10^2$  /M/s, and  $k = 2 \cdot 10^3$  /M/s. The total amount of templates was chosen as  $[T_1^{tot}] = 100$  nM,  $[T_2^{tot}] = 200$  nM. The initial conditions of active  $[T_i]$  are set as  $[T_1](0) = 10$  nM and  $[T_2](0) = 160$  nM, while  $[R_1](0) = [R_2](0) = 0$ . Example traces are shown in Figure S17 (a modified version of this figure is also in the main paper). Each product's flux rate is defined again as the derivative of  $[R_i^{tot}]$ . The flux mismatch is defined as the absolute value of the difference between the two flux rates. The effect of changing the feedback strength, where for simplicity  $\delta_1 = \delta_2$ , is shown in Figure S17 B and C, which plots the active fraction of  $[T_i]$  and the flux mismatch averaged over the last one hour of a 10 hours simulation. The right panel in Figure S17 seems to indicate that the flux mismatch of the two circuits is minimized for a certain range of  $\delta$  around the nominal value of  $\delta = 5 \cdot 10^2$ .

The nullclines of the system in the  $T_1$ - $T_2$  space can be calculated as done for the negative feedback design. Taking equations (6), we find:

$$\begin{aligned} \dot{T}_j = 0 &\implies R_i = \frac{\alpha_j T_j}{\delta_{ij} (T_j^{tot} - T_j)}, \\ \dot{R}_i = 0 &\implies R_i = \frac{\beta_i T_i}{k R_j + \delta_{ij} (T_j^{tot} - T_j)}. \end{aligned}$$

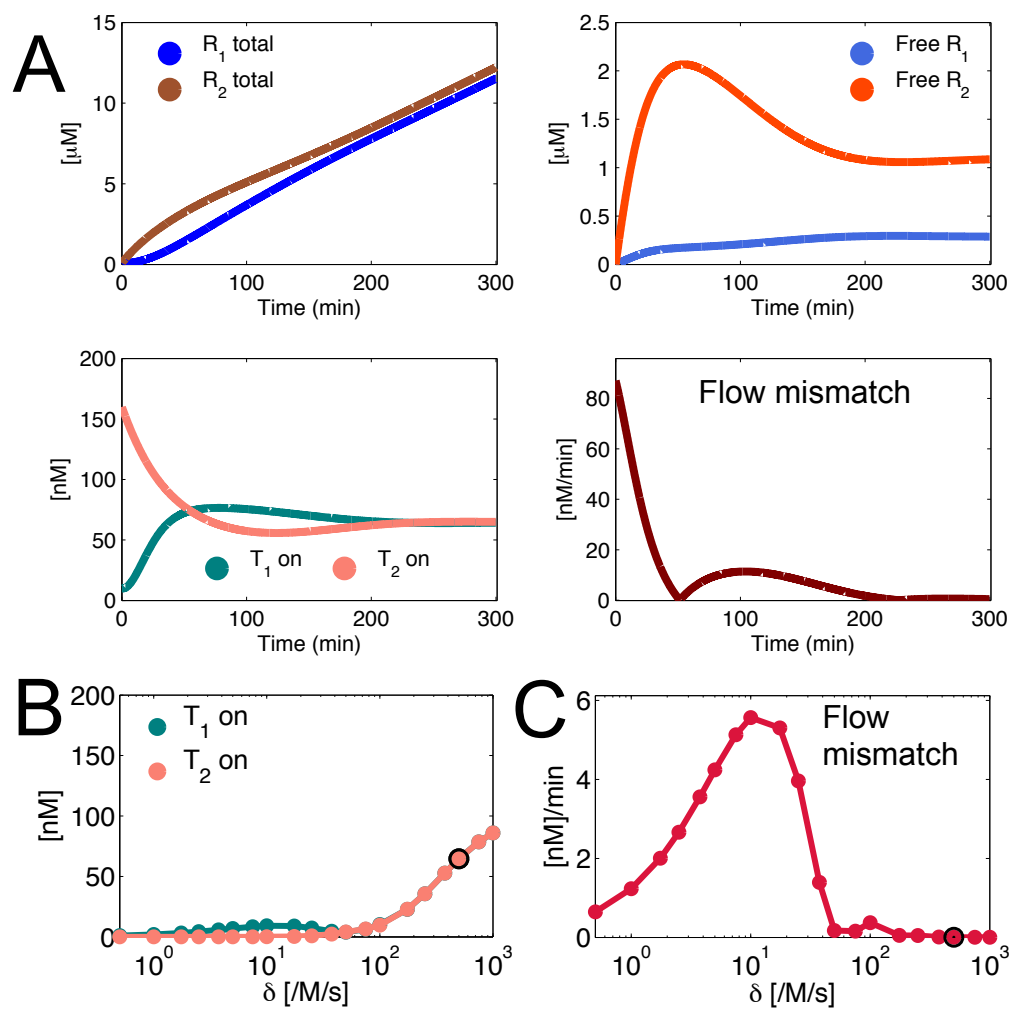


Figure S17: A: Example numerical simulation showing the time evolution of the source species in the positive feedback architecture (Figure S16 modeled with equations (6)). B: Active concentration of source species as a function of the positive feedback rate  $\delta$ . C: Flow mismatch between  $R_1$  and  $R_2$  as a function of  $\delta$ . Dark circles indicate the value of  $\delta$  used in panel A.

To simplify the derivation, we set  $\delta_{12} = \delta_{21} = \delta$ ,  $\beta_1 = \beta_2 = \beta$ ,  $\alpha_1 = \alpha_2 = \alpha$ . Equating the two expressions for  $R_i$ , we get the following equations (for  $i = 1, 2$  and  $j = 1, 2$ ):

$$\left(\frac{\alpha}{\delta}\right)^2 k \left(\frac{T_i}{T_i^{tot} - T_i}\right) \left(\frac{T_j}{T_j^{tot} - T_j}\right) + \alpha T_i - \beta T_j = 0. \quad (7)$$

We can find an expression of the nullclines by introducing a change of variables  $z = \left(\frac{T_1}{T_1^{tot} - T_1}\right)$  and  $w = \left(\frac{T_2}{T_2^{tot} - T_2}\right)$ , and defining  $\phi_1 = \psi_1 = \left(\frac{\alpha}{\delta}\right)^2 k$ ,  $\phi_2 = \alpha T_1^{tot}$ ,  $\psi_2 = \alpha T_2^{tot}$ ,  $\phi_3 = \beta T_2^{tot}$ , and finally  $\psi_3 = \beta T_1^{tot}$ :

$$z^2(\phi_1 w) + z(\phi_1 w + \phi_2 - \phi_3 \frac{w}{1+w}) - \phi_3 \frac{w}{1+w} = 0, \quad (8)$$

$$w^2(\psi_1 z) + w(\phi_1 z + \psi_2 - \psi_3 \frac{z}{1+z}) - \psi_3 \frac{z}{1+z} = 0. \quad (9)$$

The roots of the equations above represent the nullclines of the system. Because all the parameters in these equations are positive, there is always a single root. The nullclines are numerically solved, for varying  $\delta$ , in Figure S18. A condition for flow matching at steady-state can be derived as follows:

$$\begin{aligned} \dot{R}_1 - \dot{R}_2 &= 0, \\ \beta_1 T_1 - \delta_{21} R_1 (T_2^{tot} - T_2) &= \beta_2 T_2 - \delta_{12} R_2 (T_1^{tot} - T_1). \end{aligned}$$

Substituting the expressions for  $R_1$  and  $R_2$  that can be derived by setting  $\dot{T}_1 = 0 = \dot{T}_2$ , we get:

$$\beta_1 \bar{T}_1 - \frac{\delta_{21}}{\delta_{12}} \alpha_2 \bar{T}_2 = \beta_2 \bar{T}_2 - \frac{\delta_{12}}{\delta_{21}} \alpha_1 \bar{T}_1.$$

Taking  $\alpha_1 = \alpha_2 = \alpha$ ,  $\beta_1 = \beta_2 = \beta$ , and  $\delta_{12} = \delta_{21} = \delta$  we get:

$$\bar{T}_2 = \bar{T}_1. \quad (10)$$

This flow matching condition is shown in Figure S18 in the red dashed line. Decreasing  $\alpha$  (inactivation rate for the generating species) or increasing  $\delta$  (speed of the positive feedback), with respect to the nominal values chosen here, causes the equilibrium of the system to be pushed toward the upper right corner of Figure S18. Moreover, when decreasing  $\alpha$  or increasing  $\delta$  the system reaches equilibrium on a timescale in the order of several dozens of hours. Explicit tradeoffs on the effects of  $\alpha$  and  $\delta$  may be found by further analysis on the nullclines and on the locus of equilibria in equation (7).

## 4.2 A possible experimental implementation of a two-gene positive feedback scheme

The experimental implementation of our positive feedback scheme using transcriptional networks presents several challenges. Here we present its general idea. A viable strand design scheme is in

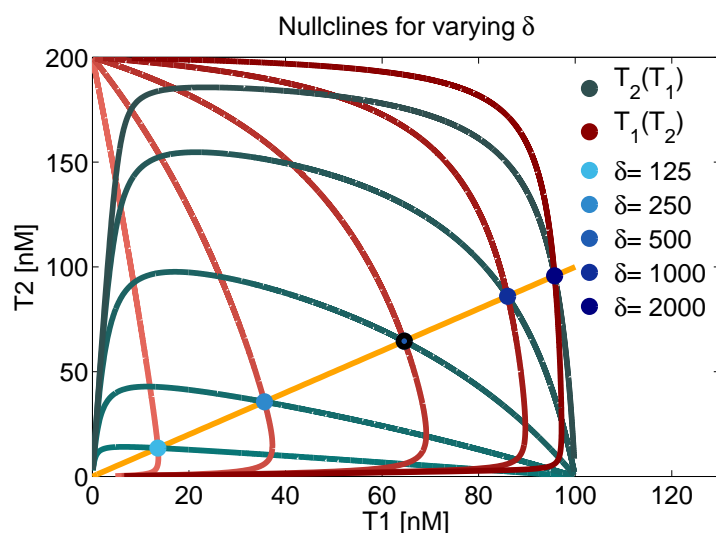


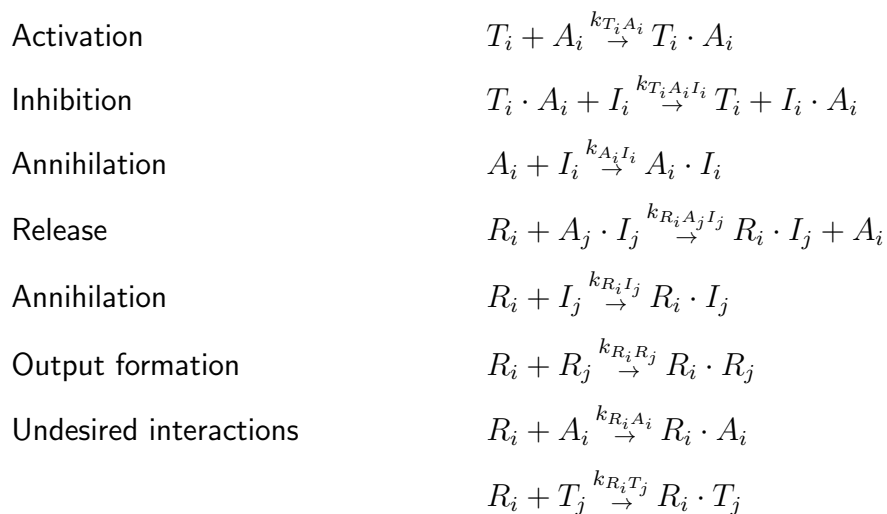
Figure S18: Numerical simulation: nullclines of the positive feedback scheme (6) in the  $T_1$ - $T_2$  plane, calculated for different values of  $\delta$  finding the roots of equations (8) and (9). The equilibrium corresponding to the set of nominal parameters (trajectories in Figure S17 A) is circled in black. The flow matching condition (10) is shown in the orange line. The flow matching condition is satisfied by the equilibria  $\bar{T}_1$  and  $\bar{T}_2$  for  $\delta = 5 \cdot 10^3$ .

Figure S19 A. Both genelets are constitutively inhibited by a DNA inhibitor  $I_i$ . Each RNA output  $R_i$  is designed to bind to the inhibitor  $I_j$  (domains indicated as  $q_j$ - $a_j$ - $t_j$ ), thereby releasing the activator  $A_j$  for binding to  $T_j$ . Because  $R_i$  should also cover the active domain of  $R_j$  in the formation of  $P$ , then  $R_i$  must also be complementary to  $A_i$  (domains  $t'_i$ - $a'_i$ - $q'_i$ ): therefore, this design is structurally affected by binding of RNA to templates (as for the self-repressing circuit), and by RNA-mediated self-inhibition loops, as shown in the reaction scheme in Figure S19 C. The entity of these design pitfalls depends on the length and sequences of the complementarity domains shared by  $R_i$  and  $R_j$ . For instance, we could avoid inserting in the RNA species the toehold sequences  $t_1$ ,  $t'_1$ ,  $t_2$ , and  $t'_2$  to minimize the self inhibition; however, this would facilitate the formation of complexes  $A_i \cdot I_i \cdot R_j$  that would slow down the release of  $A_i$ .

Preliminary experiments on this design, reported in Franco [2012], show that the issues described above are significant. In particular, the design could be improved if the self-inhibition pathways were minimized: this was attempted, without conclusive success, by increasing the concentration of DNA inhibitors, the concentration of RNase H, and by lengthening the length of toeholds for  $A_i$  and  $I_i$ . Experiments also highlighted the possibility of “leaky” transcription of inhibited switches. We refer the reader to Franco [2012], Chapter 1, for further details. Here, we only describe our numerical analysis, which suggests that the scheme has the ability to match transcription rates of two cross-activating genelets when we choose plausible reaction parameters.

#### 4.2.1 Modeling

To construct a dynamic model for the cross-activating circuit represented in Figure S19 A, we start from a list of all the chemical reactions that can occur,



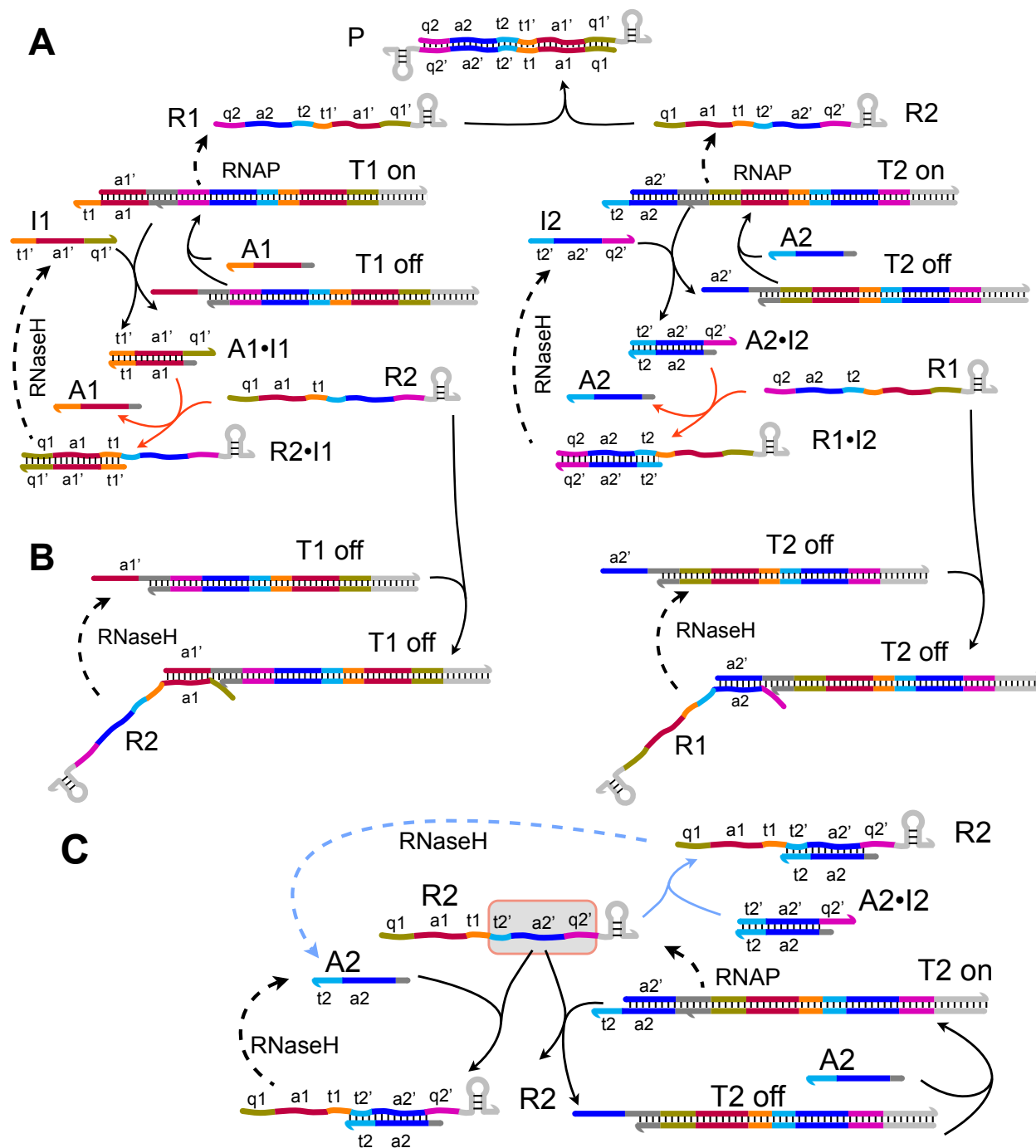
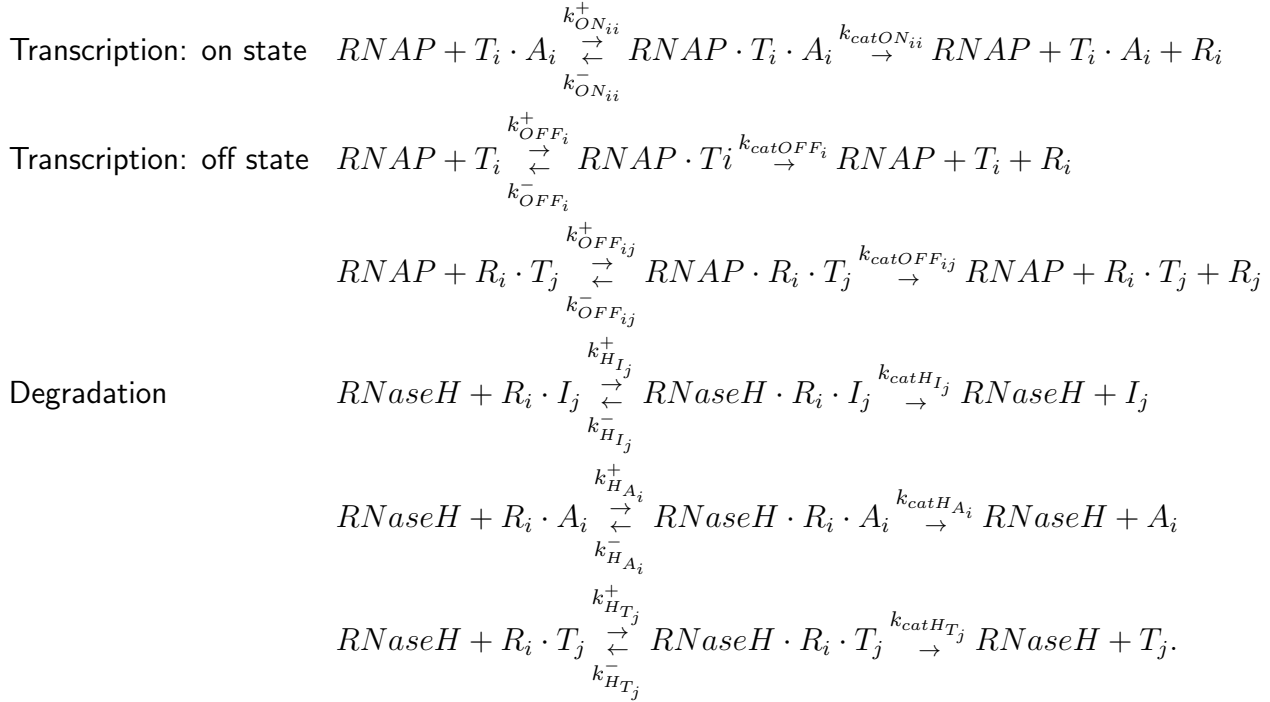


Figure S19: General reaction scheme of the transcriptional circuits implementation for the positive feedback scheme in Figure S16. Complementary domains are represented with the same color. Promoters are colored in dark gray, while hairpin terminator sequences are in light gray. A. Desired cross-activation loops. The activation reaction arrows are colored in red. B. Undesired cross-activation and RNase H-mediated degradation of the RNA-templated complexes. C. Undesired self-inhibition. The inhibition pathway in cyan arrows nominally should not occur, since there is no exposed toehold to favor it. However, this reaction has been observed in preliminary experiments not shown in this manuscript and is therefore also included in the models.



The resulting set of ordinary differential equations is:

$$\begin{aligned}
\frac{d}{dt}[T_i] &= -k_{T_i A_i}[T_i][A_i] - k_{R_j T_i}[R_j][T_i] + k_{T_i A_i I_i}[T_i \cdot A_i][I_i] + k_{catHT_i}[RNaseH \cdot R_j \cdot T_i], \\
\frac{d}{dt}[A_i] &= -k_{T_i A_i}[T_i][A_i] - k_{A_i I_i}[A_i][I_i] - k_{R_i A_i}[R_i][A_i] + k_{catHA_i}[RNaseH \cdot R_i \cdot A_i], \\
\frac{d}{dt}[I_i] &= -k_{A_i I_i}[A_i][I_i] - k_{T_i A_i I_i}[T_i \cdot A_i][I_i] - k_{R_j I_i}[R_j][I_i] + k_{catHI_i}[RNaseH \cdot R_j \cdot I_i], \\
\frac{d}{dt}[R_i] &= -k_{R_i A_j I_j}[R_i][A_j \cdot I_j] - k_{R_i R_j}[R_i][R_j] - k_{R_i T_j}[R_i][T_j] - k_{R_i I_j}[R_i][I_j] - k_{R_i A_i}[R_i][A_i] \\
&\quad + k_{catON_{ii}}[RNAP \cdot T_i \cdot A_i] + k_{catOFF_i}[RNAP \cdot T_i] + k_{catOFF_{ij}}[RNAP \cdot R_j \cdot T_i], \\
\frac{d}{dt}[R_i \cdot T_j] &= +k_{R_i T_j}[R_i][T_j] - k_{catHT_j}[RNaseH \cdot R_i \cdot T_j], \\
\frac{d}{dt}[R_i \cdot R_j] &= +k_{R_i R_j}[R_i][R_j].
\end{aligned} \tag{11}$$

As previously done for the self-inhibiting circuit model, we can express the enzyme-substrate complexes using the Michaelis-Menten approximation. For the RNAP substrate, for instance, we find:

$$[RNAP \cdot T_i \cdot A_i] = \frac{[RNAP^{tot}]}{\left(1 + \sum_{i,j} \frac{[T_i \cdot A_i]}{k_{MON_{ii}}} + \frac{[T_i]}{k_{MOFF_i}} + \frac{[R_i \cdot T_j]}{k_{MOFF_{ij}}}\right)}. \tag{12}$$

Analogous expressions can be derived for all other complexes.

Equations (11) are numerically solved using the MATLAB ode23s solver. Table S4 shows the parameters used for the simulations. Such generic parameters are consistent with those in Kim

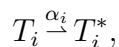
et al. [2006]. For simplicity we assume that the two sub-circuits are symmetric and have the same binding rates. We check the behavior of the system by creating an imbalance in the total concentration of inhibitors:  $[T_1^{tot}] = [A_1^{tot}] = 50$  nM,  $[T_2^{tot}] = [A_2^{tot}] = 100$  nM, while  $[I_1^{tot}] = 20$  nM and  $[I_2^{tot}] = 120$  nM. The simulation first allows for equilibration of all the DNA strands in the absence of enzymes. The plot shows the trajectories after addition of the enzymes, whose total concentration is assumed to be  $[RNAP^{tot}] = 80$  nM and  $[RNaseH^{tot}] = 8.8$  nM, based on typical experimental conditions. As noted before for the self-inhibitory scheme, the concentration of RNAP is not negligible relative to the total amount of genelets present and therefore the Michaelis-Menten approximation may not be accurate in this case. The simulation results are shown in Figure S20 and are consistent with the traces obtained for the simple model system shown at Figure S17 A: the templates cross-activate and reach an equilibrium where the flow of total RNA is matched. A comparison between the performance of the transcriptional negative and positive feedback circuits models was also done in Franco and Murray [2008].

Table S4: Parameters for the Initial Numerical Analysis of the Cross Activating Circuit

Units: $[1/M/s]$	Units: $[1/s]$	Units: $[M]$
$k_{T_i A_i} = 4 \cdot 10^4$	$k_{catON_{ii}} = 0.06$	$k_{MON_{ii}} = 250 \cdot 10^{-9}$
$k_{T_i A_i I_i} = 5 \cdot 10^4$	$k_{catOFF_i} = 1 \cdot 10^{-3}$	$k_{MOFF_i} = 1 \cdot 10^{-6}$
$k_{A_i I_i} = 5 \cdot 10^4$	$k_{catOFF_{ij}} = 1 \cdot 10^{-3}$	$k_{MOFF_{ij}} = 1 \cdot 10^{-6}$
$k_{R_j A_i I_i} = 5 \cdot 10^5$	$k_{catH_{I_i}} = 0.1$	$k_{MH_{I_i}} = 50 \cdot 10^{-9}$
$k_{R_i I_i} = 5 \cdot 10^5$	$k_{catH_{T_i}} = 0.1$	$k_{MH_{T_i}} = 50 \cdot 10^{-9}$
$k_{R_i T_j} = 1 \cdot 10^3$	$k_{catH_{A_i}} = 0.1$	$k_{MH_{A_i}} = 50 \cdot 10^{-9}$
$k_{R_i A_i} = 1 \cdot 10^3$		
$k_{R_i R_j} = 2 \cdot 10^5$		

## 5 Numerical scalability analysis of our simplified positive feedback scheme model for flux regulation

Here we report the mathematical models for positive feedback topologies in the case of  $n$  generating species  $T_i$ . This numerical study was initially outlined in Giordano et al. [2013]. The ODE systems were derived using mass action kinetics and used for the numerical simulation of the proposed topologies in the case of three-component networks. Positive feedback is implemented, as for smaller networks, with a cross-activation scheme: when an output is in excess (not used in the product formation), it increases the generation rate of all the other outputs it forms a product with:



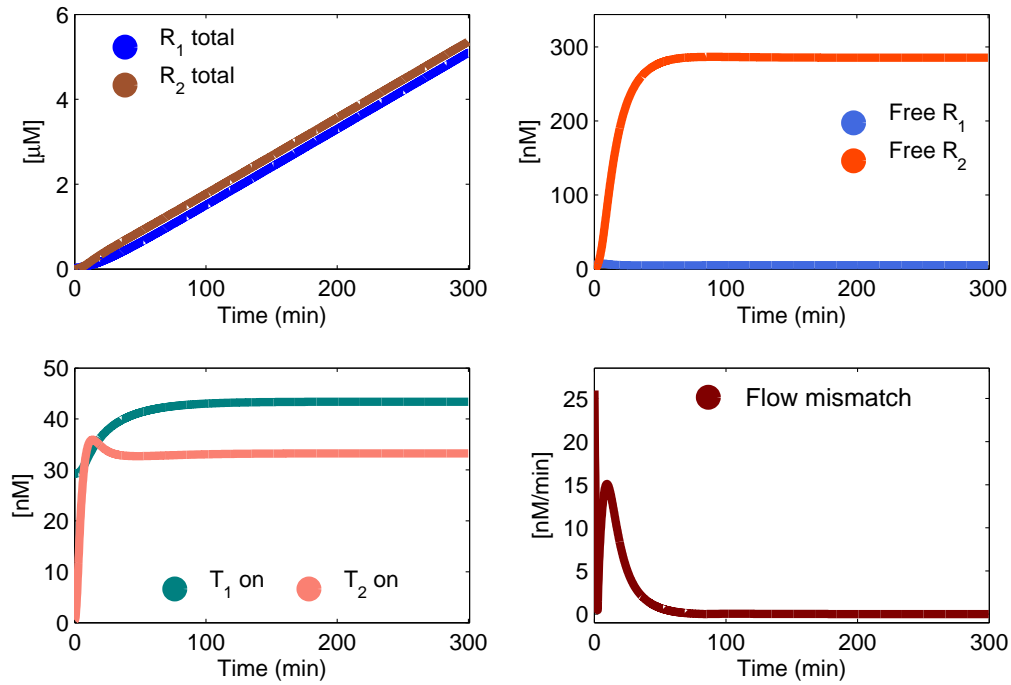
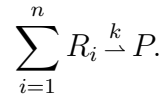


Figure S20: Numerical simulation for equations (11). Parameters are chosen as in Table S4.  $[T_1^{tot}] = [A_1^{tot}] = 50$  nM,  $[T_2^{tot}] = [A_2^{tot}] = 100$  nM, while  $[I_1^{tot}] = 20$  nM, and  $[I_2^{tot}] = 120$  nM.  $[RNAP^{tot}] = 80$  nM and  $[RNaseH^{tot}] = 8.8$  nM. These numerical results are in general consistent with those obtained for the simple model (6), shown in Figure S17 A.

where  $T_i^*$  is an inactive complex. We assume that  $[T_i^{tot}] = [T_i] + [T_i^*]$  and that the active complex  $T_i$  naturally inactivates with a first order rate  $\alpha_i$ .

## 5.1 Single product topology

In a single product topology, a single complex  $P$  is concurrently formed by all the  $n$  outputs:



The corresponding differential equations are

$$\begin{aligned} \frac{d[T_i]}{dt} &= -\alpha_i [T_i] + \delta_i ([T_i^{tot}] - [T_i]) \prod_{j \neq i} [R_j] \\ \frac{d[R_i]}{dt} &= \beta_i [T_i] - k \prod_{i=1}^n [R_i] - \delta_i [R_i] \prod_{j \neq i} ([T_j^{tot}] - [T_j]) \\ \frac{d[P]}{dt} &= k \prod_{i=1}^n [R_i] \end{aligned} \quad (13)$$

and the total amount of  $R_i$  is  $[R_i^{tot}] = [R_i] + \sum_{j \neq i} [T_j] + [P]$ . The simulation results, in Figure S21 (a), show that also this feedback strategy is effective. The concentrations of active  $T_i$

asymptotically decrease and flow mismatches reduce, yet the time response is slower than in the negative feedback case. With respect to negative feedback, there is also a higher  $R_i$  production.

## 5.2 Handshake and neighbor topologies

Subcomponents generation is expressed by the reaction  $R_i + R_j \xrightarrow{k_{ij}} P_{ij}$  and positive feedback acts on gene  $i$  due to gene  $j$ :  $R_i + T_j^* \xrightarrow{\delta_{ij}} T_j$ . The differential equations are

$$\begin{aligned} \frac{d[T_i]}{dt} &= -\alpha_i [T_i] + \sum_j \delta_{ij} [R_j] ([T_i^{tot}] - [T_i]) \\ \frac{d[R_i]}{dt} &= \beta_i [T_i] - \sum_j k_{ij} [R_i][R_j] - \sum_j \delta_{ji} [R_i] ([T_j^{tot}] - [T_j]) \\ \frac{d[P_{ij}]}{dt} &= k_{ij} [R_i][R_j] \end{aligned} \quad (14)$$

and the total amount of  $R_i$  is  $[R_i^{tot}] = [R_i] + \sum_j [T_j] + \sum_j [P_{ij}]$ . We remind that the two topologies coincide in the case  $n = 3$ . The simulation results are shown in Figure S21 (b). The concentration of active genes decreases and the flux mismatches are reduced, but the response time is still longer than in the negative feedback architecture. Moreover, there is a higher  $R_i$  production than in the negative feedback case. We can note that the handshake/neighbor connection generates less waste (unused  $R_i$ ) than the single product interconnection.

## 5.3 Parameters

For the numerical solution, the parameters chosen are:  $k_{ij} = 2 \cdot 10^3$  /M/s for the handshake/neighbor topology and  $k = 6 \cdot 10^3$  /M/s for the single product topology,  $\delta_{ij} = 50$  /M/s,  $\alpha_i = 3 \cdot 10^{-4}$  /s,  $\beta_i = 1 \cdot 10^{-2}$  /s,  $[T_1^{tot}] = 100$  nM,  $[T_2^{tot}] = 200$  nM,  $[T_3^{tot}] = 300$  nM. An imbalance in the production rates of  $R_i$  is created by setting  $[T_i](0) = [T_i^{tot}]$ , while  $[R_i](0) = 0$ .

## 5.4 Performance overview of the different topologies as a function of key parameters

Using Figures S23 and S24 as a support, we can compare the performance of the positive feedback strategy for networks with  $n = 3$ . These topologies are shown in Figure S22; for  $n = 3$  the handshake and neighbor topology coincide, Figure S22 B.

We numerically analyzed the network response in terms of active percentage of  $T_i$ , mean flow mismatch and response time, defined as previously done for negative feedback topologies. We solved the differential equations for a time span of 10 hours and averaged the trajectories for active  $T_i$  and for the computed mismatch over the last simulation hour. We examined the sensitivity to variations in  $\delta$ , the feedback strength, and in  $\alpha$ , the rate of spontaneous inactivation of  $T_i$ :  $\delta$  varies from a hundredth to a hundred times its nominal value;  $\alpha$  varies from a hundredth of its nominal value to twice its nominal value, and up to five times its nominal value in the response time analysis. In each figure, a pink square highlights the system behavior when the nominal parameters in Section 5.3 are adopted.

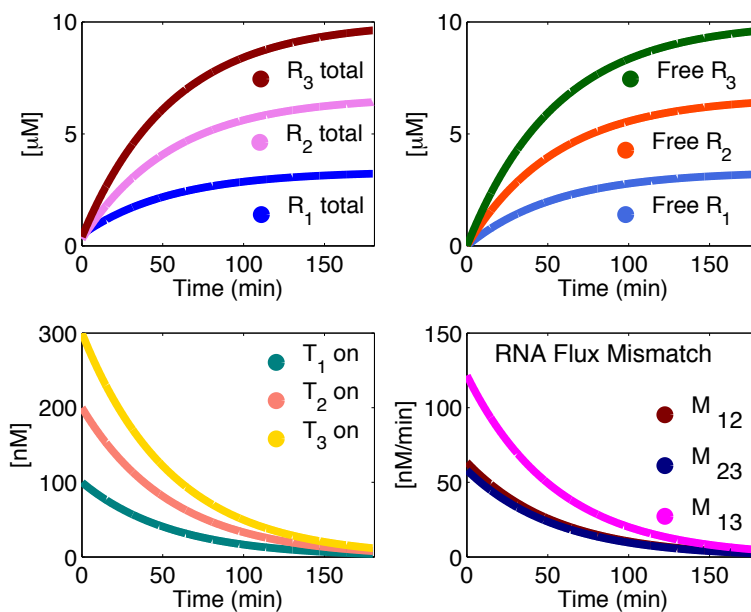
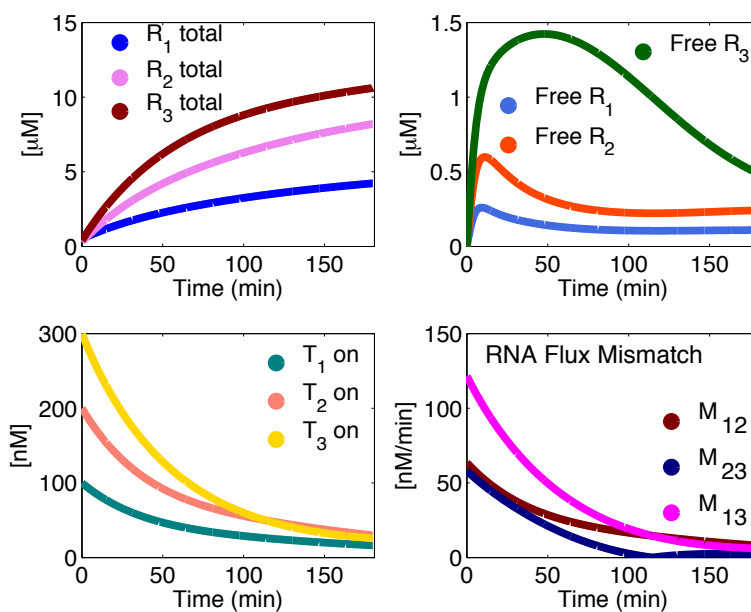
(a) single product topology,  $n = 3$ (b) handshake/neighbor topologies,  $n = 3$ 

Figure S21: Example traces from numerical simulations: positive feedback scheme.



Figure S22: A: Single product topology. B: Handshake/neighbor interconnection.

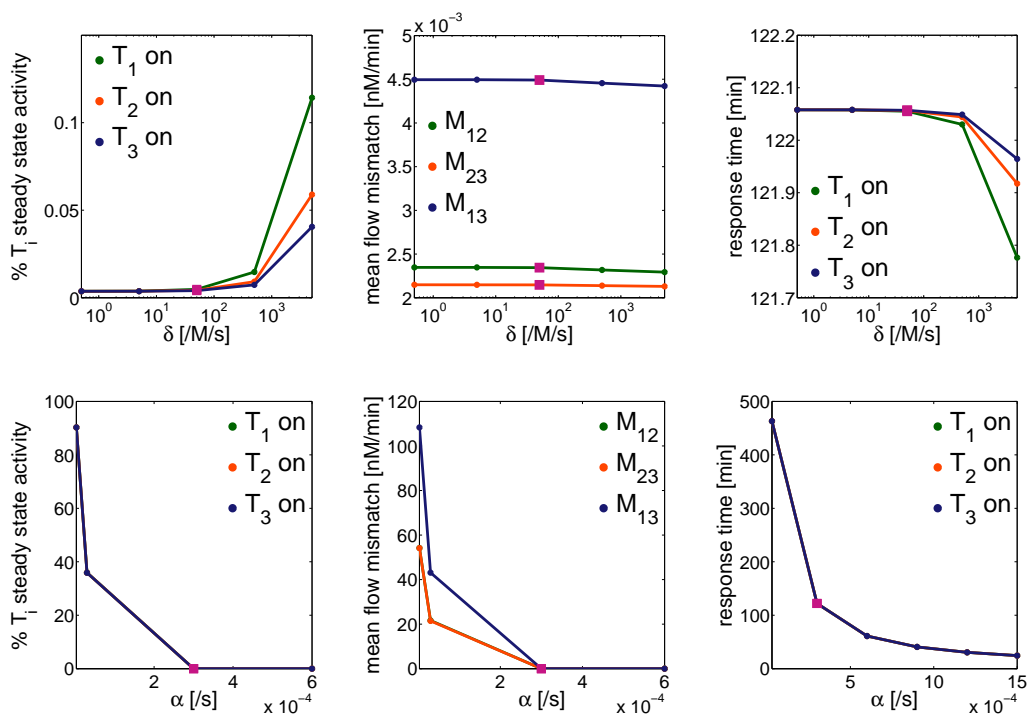


Figure S23: Positive feedback, single product topology: parameter sensitivity analysis.

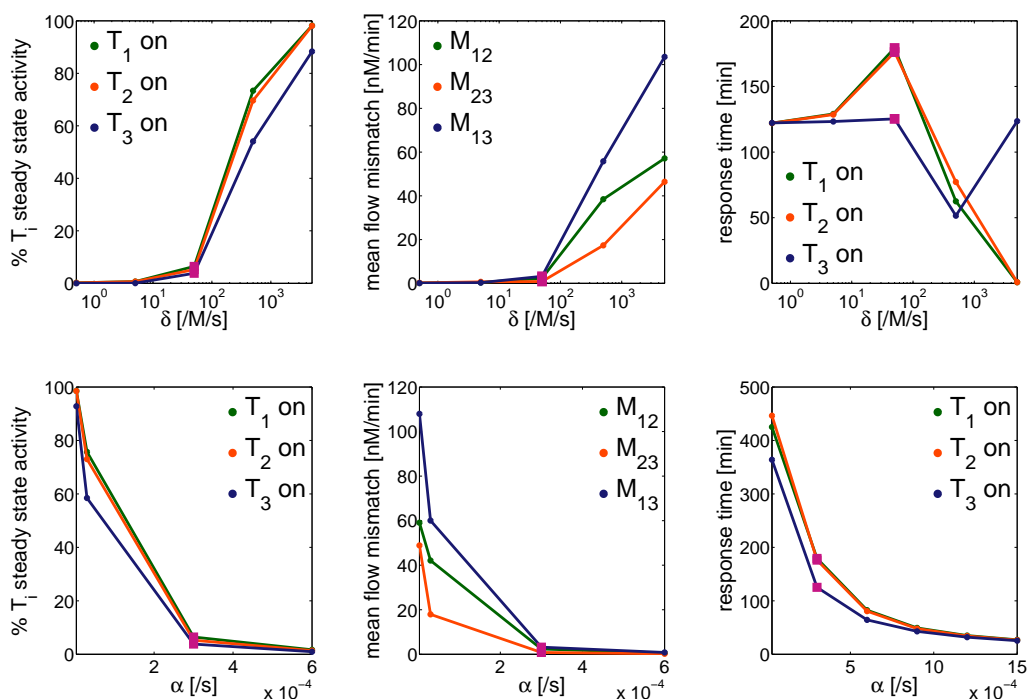


Figure S24: Positive feedback, neighbor/handshake topology: parameter sensitivity analysis.

In all network topologies, an increase in the spontaneous inactivation parameter  $\alpha$  yields a lower mismatch, decreases the response time and considerably reduces the steady state activity of  $T_i$ . In the handshake/neighbor topology, an increase in the positive feedback parameter  $\delta$  yields a significantly higher  $T_i$  steady state activity and a larger mismatch; in the single product topology, instead, the steady state activity of  $T_i$  is quite low and almost insensitive to variations in  $\delta$  and the mismatch is almost independent of  $\delta$ . When  $\delta$  increases, the response time decreases in the single product topology, while it does not have a monotone behavior in the handshake/neighbor topology.

## References

- Integrated DNA technologies: <http://www.idtdna.com>. URL <http://www.idtdna.com>.
- E. Franco. *Analysis, design, and in vitro implementation of robust biochemical networks*. PhD thesis, California Institute of Technology, 2012.
- E. Franco and R. M. Murray. Design and performance of *in vitro* transcription rate regulatory circuits. In *Proceedings of the IEEE Conference on Decision and Control*, 2008.
- E. Franco, P.-O. Forsberg, and R. M. Murray. Design, modeling and synthesis of an *in vitro* transcription rate regulatory circuit. In *Proceedings of the American Control Conference*, 2008.
- E. Franco, E. Friedrichs, J. Kim, R. Jungmann, R. Murray, E. Winfree, and F. C. Simmel. Timing molecular motion and production with a synthetic transcriptional clock. *Proceedings of the National Academy of Sciences*, 108(40):E784–E793, 2011.
- G. Giordano, E. Franco, and R. M. Murray. Feedback architectures to regulate flux of components in artificial gene networks. In *Proceedings of the American Control Conference*, 2013.
- J. Kim. *In vitro synthetic transcriptional networks*. PhD thesis, California Institute of Technology, 2007.
- J. Kim and E. Winfree. Synthetic *in vitro* transcriptional oscillators. *Molecular Systems Biology*, 7:465, 2011.
- J. Kim, K. S. White, and E. Winfree. Construction of an *in vitro* bistable circuit from synthetic transcriptional switches. *Molecular Systems Biology*, 1:68, 2006.
- S. Milburn, M. Goldrick, and M. Winkler. Compositions and methods for increasing the yields of *in vitro* RNA transcription and other polynucleotide synthetic reactions, U. S. Patent 5256555, 1993.
- J. N. Zadeh, C. D. Steenberg, J. S. Bois, B. R. Wolfe, M. B. Pierce, A. R. Khan, R. M. Dirks, and N. A. Pierce. NUPACK: analysis of nucleic acid systems. *Journal of Computational Chemistry*, 32:170–173, 2011.
- M. Zuker and P. Stiegler. Optimal computer folding of large RNA sequences using thermodynamics and auxiliary information. *Nucleic Acids Research*, 9(1):133–148, 1981.